A Maximum-Likelihood Energy Reconstruction Method

Pol d'Avezac, LLR, Ecole polytechnique

February 9, 2006

1 Introduction

The LAT is expected to measure the direction and primary energy of photons ranging from 20 MeV to over 300 GeV over a 2.5 sr solid angle. It is composed of 16 towers. Each of them has a CsI calorimeter (CAL), of a thickness of 8.6 radiation lenghts along the z-axis, over which sits a tracker (TKR), of a thickness of 1.3 radiation length. The CAL is designed to measure the primary energy of the photons (E_γ). Because of matter upstream of the CAL and its relatively small depth, the total energy deposit in the CAL is rarely by itself a reliable measure of E_γ. Its understanding is further complicated by the large solid angle in which photons are observed. For these reasons, energy reconstruction methods are developped, adapted to different configurations.

The method presented in this note, named CalLikelihood, reconstructs primary energies in the range of 50 MeV to 300 GeV and within 49 ° of the vertical for photons converting in the TKR and for which the latter reconstructs a direction. The method could in principle be extended to energies above and angles beyond these given ranges, as well as to events converting in the CAL.

The principles of physics underlying the analysis are presented in section 2. The reconstruction itself is based on a maximum-likelihood method. The probability density function (PDF) which it will use and the observable which it describes is explained in section 3.1. Because of the complexity of the LAT phase-space, a large number of PDFs will be constructed corresponding to as many different classes of events. The latters are defined in 4. Lastly, the reconstruction method itself, and a study of its performance, is given in 5.

2 Basic Principles: LAT versus Shower Geometry

The instrument primarily uses the measurement of the total energy deposition in the CAL (Q_γ) to reconstruct E_γ. This measurement is classically affected by noises such as photon statistics or electronic noise, for which little can be done (0.4 MeV/crystal for crystal

energy deposits $< 100\,\mathrm{MeV}$, $10\,\mathrm{MeV}$/crystal for crystal energy deposits $> 1\,\mathrm{GeV}$). Other parameters come into play which are the result of both the shape of the energy deposit and the geometry of the LAT.

The energy deposit is pear-shaped, this because in the GLAST energy range, photons interact with matter mainly by creating a shower of electrons, positrons and photons of lesser energy. The shower posesses a rotational symetry around its direction, this because of momentum conservation and the large number of created particles. The average shower energy density profile can be factorised in a longitudinal times a radial distribution [5]. Shower containment in the CAL, defined here as $\delta_\gamma = \frac{Q_\gamma}{E_\gamma}$, should thus be described with parameters specific to the longitudinal or the lateral development of the pear-shaped shower.

The geometry of the LAT itself is cubic: rows of crystals or strips, layers stacked upon layers. It is not adapted to the shape of the showers unless in the case of on-axis photons. For off-axis photons, the energy sampling performed by the CAL crystals will suffer from a mixing of the lateral and longitudinal shower parameters. Using spherical coordinates to describe the shower direction, the polar angle is the angle between the photon direction and the vertical (noted θ for the Monte-Carlo truth, $\tilde{\theta}$ for the TKR-reconstructed value). The azimuthal angle lies in the horizontal plane defined by the crystal layers. Both are characteristic of this mixing. Although the azimuthal angle affects the measurements performed by the crystals, the impact on the sum in one layer, the total energy deposit measurement in one layer, is mainly averaged out. In this analysis, the azimuthal angle is ignored; the effect will implicitly be taken into account through the calibration of the method. The mixing effect is thus solely described using θ. It will not be addressed before section 4. In other words, until then, longitudinal shower parameters will effectively characterize longitudinal energy leaks, whereas lateral shower parameters will characterize lateral energy leaks.

2.1 Lateral Shower Parameters

A few constants and observables must first be defined to understand the effect of the lateral leaks. To describe the physics of the shower, the Moliere radius ($R_M = 38\,\mathrm{mm}$ in CsI) is used as the radial scale. Just as for the radiation length, it depends solely on the matter encountered by the shower [6]. 90% of the energy is contained within a cylinder of revolution the shower axis and of radius R_M. In comparison, the CAL crystal width is $0.73\,R_M$. To describe the position of the shower in the CAL, an observable is defined. It uses the CAL reconstructed energy centroid. The centroid is defined as the mean of the reconstructed shower position in each crystal, weighted by the crystal energy. In each crystal, the position is reconstructed using the light taper (30% for one crystal, end-to-end). D_{cracks} is the distance to vertical edges of the tower containing the centroid. It ranges from $0\,\mathrm{mm}$, outside the CAL crystals to $187.25\,\mathrm{mm}$, the core of the tower. For $D_{\mathrm{cracks}} \in [0\,\mathrm{mm}, 22\,\mathrm{mm}]$, the centroid sits outside the active material in the tower. This is the tower gap. For $D_{\mathrm{cracks}} > 34\,\mathrm{mm}$, its sits at least half a crystal width away from the gap, inside the layers of crystal. Anything below $34\,\mathrm{mm}$ is characteristic of an event crossing two towers. In such a case, part of the shower developped outside the active material in the CAL, not registering in Q_γ.

The effect of lateral energy leaks on shower containment is illustrated in Fig. 1 which

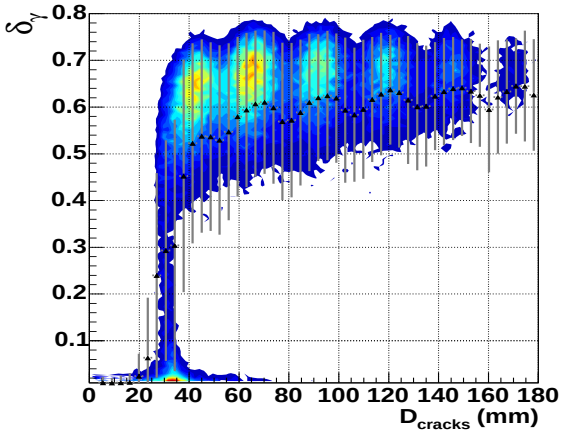

Figure 1: Q_γ versus D_{cracks} for $E_\gamma = 10\,\text{GeV}$, $\theta = 0\,°$. The error bars indicate the mean and spread of the distribution.

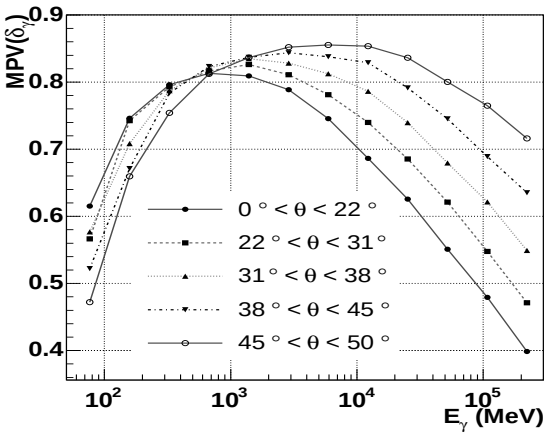

Figure 2: $\frac{Q_\gamma}{E_\gamma}$, versus E_γ for various ranges of θ. A transition is visible from TKR to bottom of CAL leaks.

shows this parameter versus D_{cracks}. Tower gaps are responsible for the dramatic loss in shower containment at $D_{\text{cracks}} = 34\,\text{mm}$. The gaps affect the showers for about 1 R_M. Cracks in between crystals are responsible for the less dramatic loss in shower containment; this feature quickly disappears with increasing θ and is ignored. As can be seen, the shower containment quickly stabilises to about 0.65, 1 R_M inside the active part of the CAL. Above 60 to 80 mm, the lateral leaks are negligeable.

This method does not directly correct for loss in shower containment visible below 80 mm. Because the crystal width is comparable to R_M, the core of the shower fits into two or three crystals. Such a coarse sampling, illustrated in Fig. 1, means that little information is to be had from the lateral profiles and as such on the importance of lateral leaks. Although other methods, such as CalFullProfile [2], try to quantify these by using the radial profile, this one does not. As a result, the effect of tower gaps is to smear any correlations between the LAT observables and the Monte-Carlo truths. It drasticly lowers the amount of information in the LAT observables. For this reason, this method defines various event classes, based on geometric cuts, for different qualities of events. This will be shown in section 4. Until then, figures are created with events for which containement is not affected by the tower gaps.

2.2 Longitudinal Shower Parameters

The longitudinal developpment of showers will also affect the measure of Q_γ. Mainly two effects can be observed. Showers may not extend up to the CAL because of the matter upstream, the TKR. This is the case for low energy photons. Shower may also extend too far, in which case leaks occur through the bottom of the CAL. Fig. 2 shows the transition from one regime to the other. It occurs around 2 GeV. At that energy, for on-axis photons, about 5% of shower energy will escape through the bottom of the CAL. Because of this, the observable Q_γ is not an effective measurement to estimate E_γ. The reconstruction corrects for these leaks by defining a new observable X_L. This is shown in section 3.1.

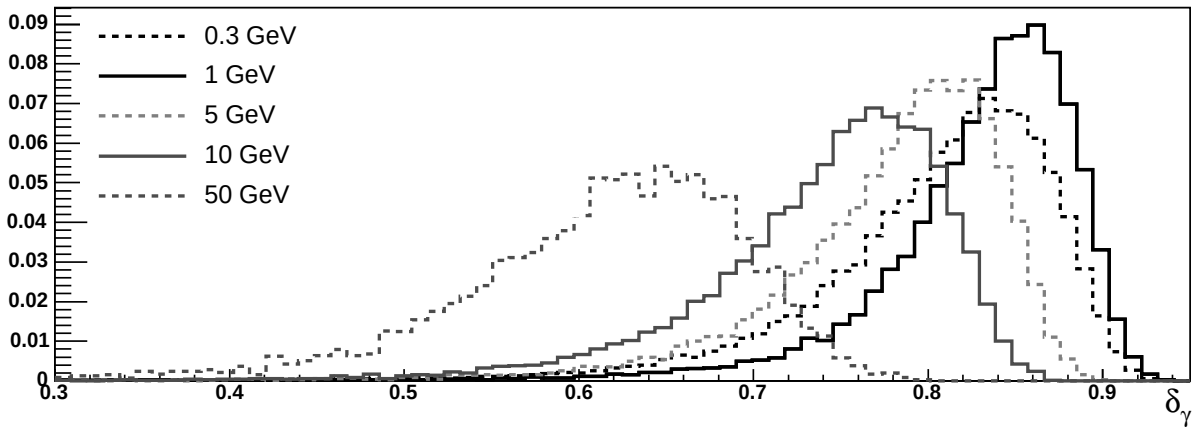

Figure 3: probability distributions for Q_γ, with $\theta = 32\,^\circ$.

3 Creating the PDFs

The definition of the X_L observable is given in section 3.1. It must be optimised, this is shown in section 3.2. Finally, defining an estimation of the X_L PDFs is done in section 3.3.

3.1 A new observable: X_L

The most straight-forward measure of a photon's primary energy is Q_γ. A reconstruction method using this sole observable would have at best a resolution equal to the variance of the Q_γ distribution at that energy. Fig. 3 shows shower containment distributions, normalised so as to behave like a probability distribution, for photons with a $32\,^\circ$ incidence at 300 MeV, 1, 5, 10, and 50 GeV. Because of the longitudinal effects described in section 1, these distributions have varying tails and RMS depending on E_γ. Thus the response function is non gaussian. Furthermore, the most probable values (MPV) don't have the same values, affecting the linearity of the response function. The last layer method [8][7], of which this method is an extension, defines a new observable X_L for which the same probability distributions will have lower RMS as well as a greater linearity.

The variance of the Q_γ distribution at a fixed E_γ value results from the fluctuations in the development of the shower. Even with the same starting point in the TKR, direction and initial energy, showers may not develop strictly in the same way, losing a varying amount of energy in the TKR, leaking different amounts of energy through the CAL bottom. The variance of Q_γ due to this effect may be corrected using other observables which will correlate positively with the missing energy. Such observables should correspondingly anti-correlate with Q_γ. In such a way, an event with Q_γ fluctuating to lower energies will be corrected by the observables as, generally, these will correspondingly fluctuate to higher values.

In order to correct for the energy leaked through the bottom of the CAL, the last layer method [8] used q_7, the energy deposit in the CAL's last layer. Hereafter we will define the energy deposited in the i-th layer as q_i. Note that $\Sigma q_i = Q_\gamma$. q_7 is correlated to the energy loss through the bottom of the CAL, this as long as the shower maximum has been reached

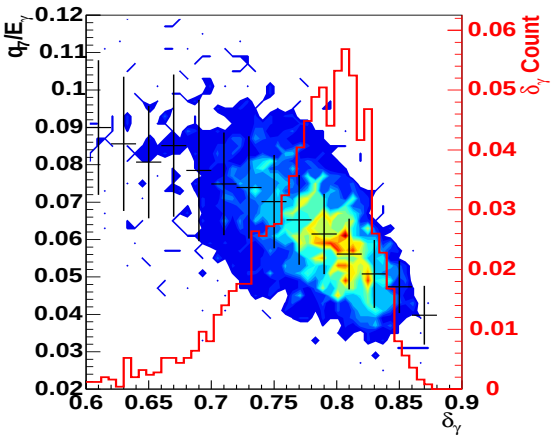

Figure 4: Q_γ versus q_7, for $E_\gamma = 10\,\text{GeV}$, $\theta = 32\,°$, events at the center of the tower, and vertexes in the bottom of the TKR. The red curve is the Q_γ distribution. This shows a clear anti-correlation between fluctuations in $Q_\gamma$and fluctuations in q_7.

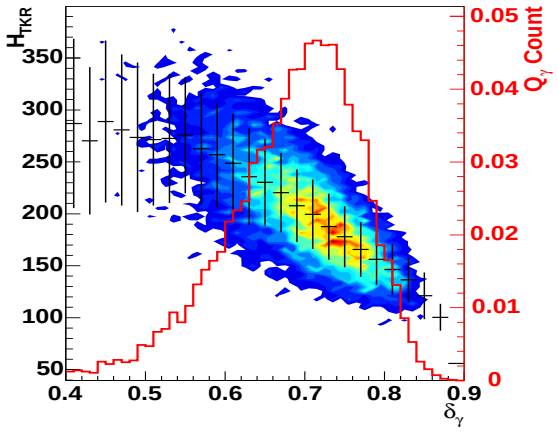

Figure 5: Q_γ versus H_{TKR}, for $E_\gamma = 1\,\text{GeV}$, $\theta = 49\,°$, events at the center of the tower, and vertexes in the bottom of the TKR. The missing energy and the number of TKR hits clearly correlate.

inside the CAL. After the shower maximum, the electron population is very much at the critical energy ($E_c = 30\,\text{MeV}$ in CsI). In other words energy deposit in the last layer happens for a decreasing population of electrons with a similar energy. q_7 is thus characteristic of the number of electrons leaving the CAL. Thus q_7 is proportional to the energy leak. This anti-correlation is illustrated on Fig. 4 for 10 GeV photons. The curve is the distribution of Q_γ. It shows how the events in the tail of that distribution correspond to higher q_7 values. adding q_7 to Q_γ should thus result in the lower tail of the $Q_\gamma$distribution catching up with its core. This should improve both the distribution's width and its asymetry. The last layer method used $Q_\gamma + \alpha \cdot q_7$, where the paramater α was optimized to correlate with the energy leak.

The last layer method worked only for $E_\gamma > 1\,\text{GeV}$, below which there are no leaks through the bottom of the CAL to correct for. The present method adds another term to the previous expression to obtain:

$$X_L = Q_\gamma + \alpha \cdot q_7 + \beta \cdot H_{\text{TKR}} \tag{1}$$

where H_{TKR} is the number of hit strips in the TKR. Especially for low energy photons, the energy absorbed by the TKR can be an important fraction of the energy missing in the CAL. The method will correct for this by applying a correction factor to the energy in the CAL times the number of hit strips. Fig. 5 shows such a correlation, again for a given photon energy and direction. As before, events in the tail of the Q_γ distribution correspond to higher H_{TKR} values.

3.2 Optimizing the Weights

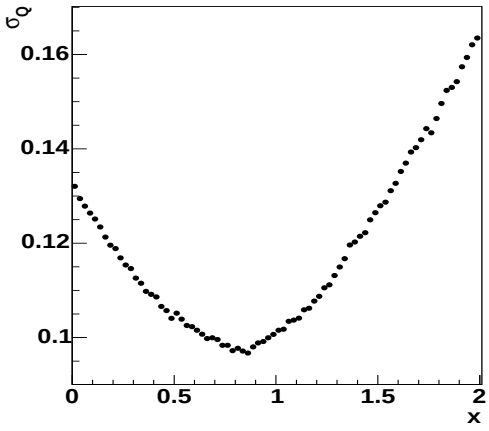

Figure 6: $\sigma_{\mathbf{Q}}$ versus x, for $E_\gamma = 300\,\mathrm{MeV}$, $\theta = 32\,^\circ$ and $\mathbf{Q}(x) = Q_\gamma + x \cdot H_{\mathrm{TKR}}$. There is a clear local minimum at $x = 0.82$, showing a gain of 37.5% in width.

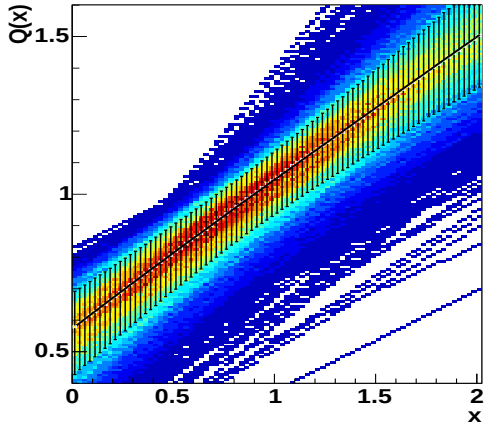

Figure 8: $\mathbf{Q}(x) = Q_\gamma + x \cdot H_{\mathrm{TKR}}$ versus x, for $E_\gamma = 300\,\mathrm{MeV}$, $\theta = 32\,^\circ$. Error bars show the FWHM values, and the color code the bin population.

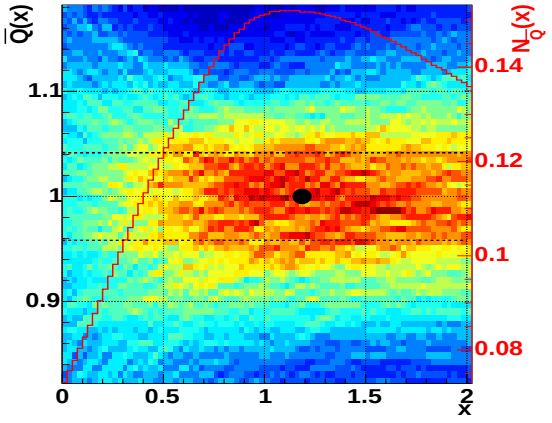

Figure 10: $\bar{\mathbf{Q}}$ versus x, for $E_\gamma = 300\,\mathrm{MeV}$, $\theta = 32\,^\circ$ and $\mathbf{Q}(x) = Q_\gamma + x \cdot H_{\mathrm{TKR}}$. The red curve is $N_{\bar{\mathbf{Q}}}$. The dotted lines show the RMS used to produce it. The marker indicates β.

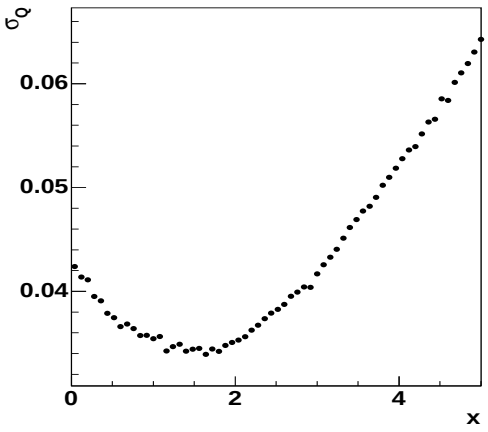

Figure 7: $\sigma_{\mathbf{Q}}$ versus x, for $E_\gamma = 10\,\mathrm{GeV}$, $\theta = 32\,^\circ$ and $\mathbf{Q}(x) = Q_\gamma + x \cdot q_7$. There is a clear local minimum at $x = 1.55$, showing a gain of 25.% in width.

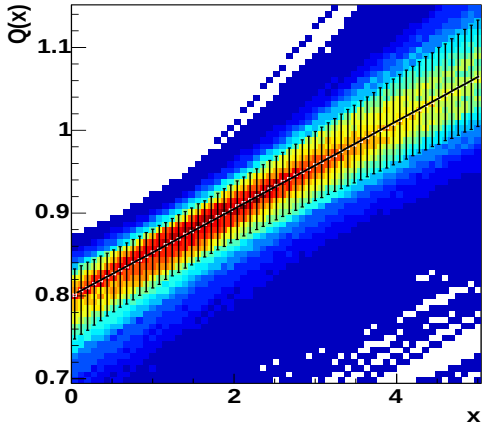

Figure 9: $\mathbf{Q}(x) = Q_\gamma + x \cdot q_7$ versus x, for $E_\gamma = 10\,\mathrm{GeV}$, $\theta = 32\,^\circ$. Error bars show the FWHM values, and the color code the bin population.

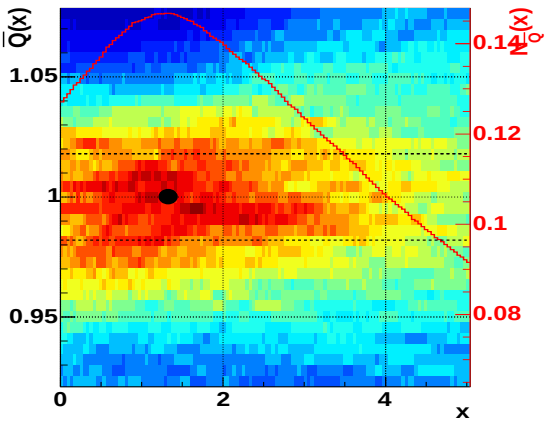

Figure 11: $\bar{\mathbf{Q}}$ versus x, for $E_\gamma = 10\,\mathrm{GeV}$, $\theta = 32\,^\circ$ and $\mathbf{Q}(x) = Q_\gamma + x \cdot q_7$. The red curve is $N_{\bar{\mathbf{Q}}}$. The dotted lines show the RMS used to produce it. The marker indicates α.

Optimising one Weight The impact of the weights upon the X_L variance, for a fixed E_γ value, will now be presented. The optimization of the weights is performed by extensively calculating the effect of the weights over a certain range and the best value chosen from there. This is shown for 300 MeV and 10 GeV and $\theta = 32\,^\circ$, for the partial sums:

$$\mathbf{Q}(x) = Q_\gamma + x \cdot H_{\mathrm{TKR}} \tag{2}$$

and

$$\mathbf{Q}(x) = Q_\gamma + x \cdot q_7 \tag{3}$$

respectively on Fig. 6 and 7. The resolution is estimated as the full-width-half-maximum (FWHM) of the $\mathbf{Q}$ distributions, normalised to the position of their maximum , i.e. $\sigma_{\mathbf{Q}} = \frac{\mathrm{FWHM}(\mathbf{Q})}{\mathrm{MPV}(\mathbf{Q})}(x)$, as a function of x, on Fig. 8 and 9. The error bars report the FWHM. The optimal weight corresponds to the minima on Fig. 8 and 9.

Looking the distributions on Fig. 10 and 11, these are the same as the previous ones on Fig. 8 and 9 respectively, only with their MPV normalised to 1. We now have $\bar{\mathbf{Q}}(x) = \frac{\mathbf{Q}}{\mathrm{MPV}(\mathbf{Q})}(x)$. The optimization could now be carried out by estimating the FWHMs directly from there. In fact, rather than calculating the dispersion of the events as a function of x, the approach is to measure the quality of the reconstruction as a function of x. This is done in the same manner as in the reconstruction analysis performed by W. Atwood (see [1]). In this analysis, the quality of a reconstruction method is defined, for a given configuration, as the number of events with the reconstructed energy ($\tilde{E}_\gamma$) within an accepted range of their Monte-Carlo truth. This number is normalised to the total number of entries. As such the value is the probability for the reconstruction of being correct. The optimal reconstruction algorithm is the one with the highest probability. In the present case, every different weight can be considered a different reconstruction. Note that this is not a true reconstruction as an unbiasing mechanism has yet to be put in place. We are for the moment only interested in reducing the variance. The accepted range of good events, or quality cut, is materialised by the horizontal dotted lines on Fig. 10 and 11. The number of counts in between them, the number of events making the cut, is shown as a red curve on either figures. This count curve is thereafter refered to as $N_{\bar{\mathbf{Q}}}(x)$. The MPV, the optimal x value, is used as α and β in equations 3 and 2: α or β. The corresponding $\bar{\mathbf{Q}}(\alpha)$, $\bar{\mathbf{Q}}(\beta)$ distributions have the smallest variance, as illustrated on the corresponding figures. The range, the width between the lines, is estimated recursively as the RMS of the $\bar{\mathbf{Q}}(x)$ distributions around the optimal value as follows:

1. Projection of the $\bar{\mathbf{Q}}(x)$ distributions on the y-axis. The range is its RMS. A first $N_{\bar{\mathbf{Q}}}(x)$ is produced with it and an estimation x_1 of the best value found.

2. Projection of the $\bar{\mathbf{Q}}(x)$ distributions on the y-axis, for $x \in [x_1 - 0.1, x_1 + 0.1]$. The range is its RMS. A second $N_{\bar{\mathbf{Q}}}(x)$ is produced and either α or β is found.

Note that between the initial definition of the weights using $N_{\bar{\mathbf{Q}}}$ and the final one using $N_{\bar{\mathbf{Q}}}$, their value may somewhat vary. On Fig. 6, using $\sigma_{\mathbf{Q}}$ we have $\beta = 0.82$. Yet the final result, on Fig. 10, using $N_{\bar{\mathbf{Q}}}$, has $\beta = 1.2$. This is due to the asymetry of the $\mathbf{Q}$ distributions which is not taken into account similarly for both definitions.

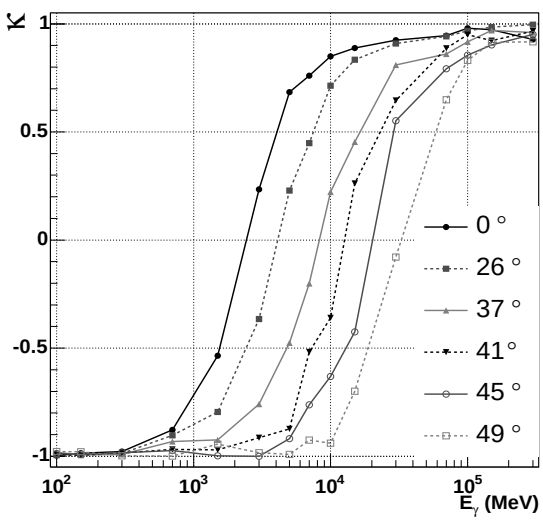

Figure 12: κ versus E_γ for various angles. The transition from the E_γ range where H_{TKR} has an impact ($\kappa < 0.$) on the variance to the one where q_7 does ($\kappa > 0.$) is visible.

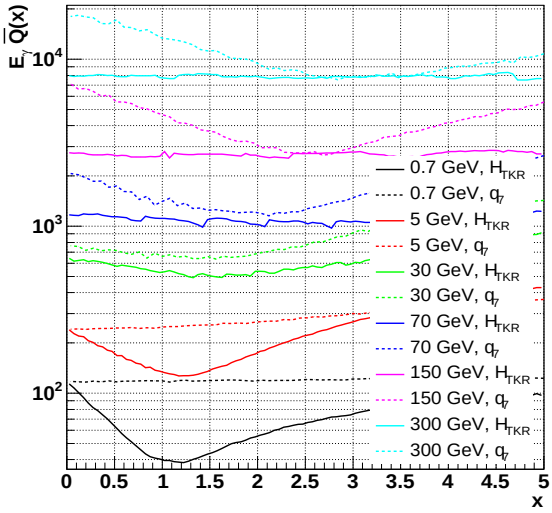

Figure 13: $\sigma_{\mathbf{Q}}$ versus x for $\theta = 49\,°$. Solid lines show the iteration on H_{TKR} for finding β. Dotted lines show the iteration on q_7 for finding α. A minimum is found for either or both H_{TKR} and q_7 at every E_γ value.

The optimization of the weights must be performed on a large number of event classes (see section 4). Becauses of this, a large amount of events must be simulated. In order to reduce the necessary statistics, a refinement is performed on the estimation of $N_{\bar{\mathbf{Q}}}(x)$. Mathematically, for one $\bar{\mathbf{Q}}(x)$ distribution, counting up the events within the said range corresponds to integrating that distribution using a step function for a kernel. A further improvement is to use a gaussian. In this way, all events are taken into account, if not with the same importance. It therefore removes the noise due to random bunching of events. This results in a smoother counting curve. This is actually the red distributions on Fig. 10 and 11. The width of the gaussian is estimated recursively as previously stated.

Optimising both Weights As pointed out in section 2, the H_{TKR} and q_7 observables are efficient in different energy ranges. The advantage of optimizing for both observables at the same time is that it removes the need to select between 2 reconstructions (one for H_{TKR}, one for q_7). Also, there could not be a smoother mechanism to translate from one range where H_{TKR} is efficient to one where q_7 is, ranges which actually overlap. Fig. 12 illustrates the translation from one correction to the other. $\Delta_{q_7} = FWHM(x = 0.) - FWHM(\alpha)$ is the gain in distribution widths obtained applying the q_7 correction. $\Delta_{H_{\mathrm{TKR}}}$ is its H_{TKR} equivalent. Thus the asymetry $\kappa = \frac{\Delta_{q_7} - \Delta_{H_{\mathrm{TKR}}}}{\Delta_{q_7} + \Delta_{H_{\mathrm{TKR}}}}$ indicates the strength of one correction versus the other. The transition occurs for the ratio equal to 0.

The optimization is carried out for both correlation parameters q_7 and H_{TKR}, in that order for high energies, in the other for low energies. In other words, in the case of high

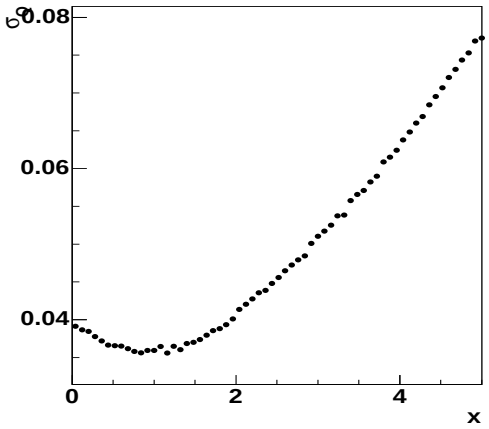

Figure 14: $\sigma_{\mathbf{Q}}$ versus x, for $E_\gamma = 5\,\mathrm{GeV}$, $\theta = 32\,^\circ$ and $\mathbf{Q}(x) = Q_\gamma + x \cdot q_7$. There is a clear local minimum at $x = 1.$, showing a gain of 5% in width.

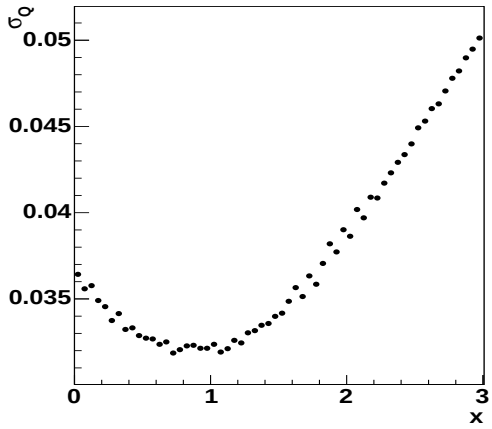

Figure 15: $\sigma_{\mathbf{Q}}$ versus x, for $E_\gamma = 5\,\mathrm{GeV}$, $\theta = 32\,^\circ$ and $\mathbf{Q}(x) = Q_\gamma + \alpha \cdot q_7 + x \cdot H_{\mathrm{TKR}}$. There is a clear local minimum at $x = 0.8$, showing a gain of 15% in width.

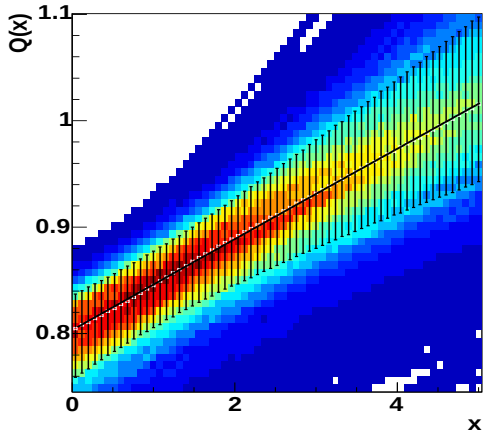

Figure 16: $\mathbf{Q}(x) = Q_\gamma + x \cdot q_7$ versus x, for $E_\gamma = 5\,\mathrm{GeV}$, $\theta = 32\,^\circ$.

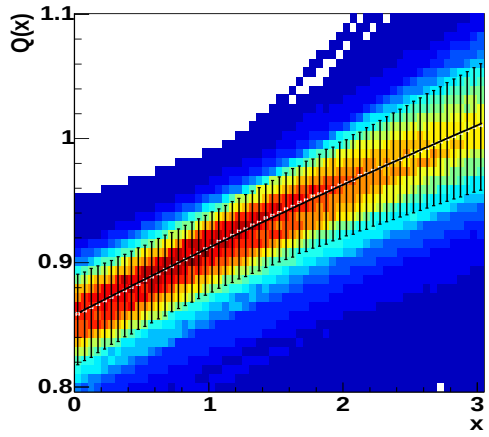

Figure 17: $\mathbf{Q}(x) = Q_\gamma + \alpha \cdot q_7 + x \cdot H_{\mathrm{TKR}}$ versus x, for $E_\gamma = 5\,\mathrm{GeV}$, $\theta = 32\,^\circ$.

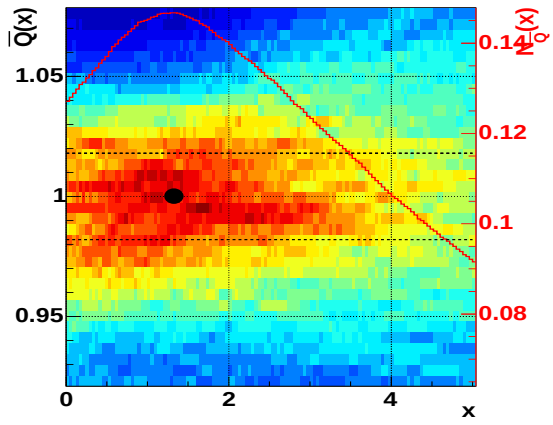

Figure 18: $\bar{\mathbf{Q}}$ versus x, for $E_\gamma = 5\,\mathrm{GeV}$, $\theta = 32\,^\circ$ and $\mathbf{Q}(x) = Q_\gamma + x \cdot q_7$.

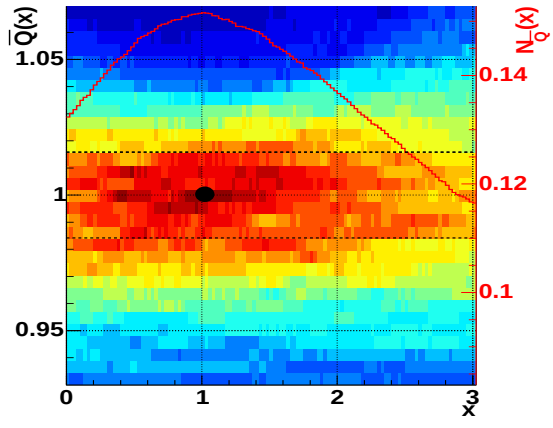

Figure 19: $\bar{\mathbf{Q}}$ versus x, for $E_\gamma = 5\,\mathrm{GeV}$, $\theta = 32\,^\circ$ and $\mathbf{Q}(x) = Q_\gamma + \alpha \cdot q_7 + x \cdot H_{\mathrm{TKR}}$.

energies, the optimization is carried out using the distributions:

$$\mathbf{Q}(x) = Q_\gamma + x \cdot q_7 \tag{4}$$

then

$$\mathbf{Q}(x) = Q_\gamma + \alpha \cdot q_7 + x \cdot H_{\mathrm{TKR}} \tag{5}$$

In this way, results can only be improved the second time around. Although this not a true 2-dimensional minimisation, it is expected that q_7 and H_{TKR} are physically sufficiently uncorrelated for the calculated values to sit close to the absolute minimum. This process is illustrated for 10 GeV, 32 ° photons in:

- Figs.14, 16 and 18, for q_7.
- Figs.15, 17 and 19, for H_{TKR}.

The overlap between ranges of usefulness for H_{TKR} and q_7 is visible on Fig. 13. It shows the $\frac{FWHM(\mathbf{Q})}{MPV(\mathbf{Q}}(x) \cdot E_\gamma$ curves for increasing energies. $\mathbf{Q}$ corresponds to the distributions:

- For solid lines, iteration with H_{TKR}:
  - For $E_\gamma \leq 1\,\mathrm{GeV}$: $\mathbf{Q}(x) = Q_\gamma + x \cdot H_{\mathrm{TKR}}$.
  - For $E_\gamma > 1\,\mathrm{GeV}$: $\mathbf{Q}(x) = Q_\gamma + \alpha \cdot q_7 + x \cdot H_{\mathrm{TKR}}$.
- For dotted lines, iteration with q_7:
  - For $E_\gamma \leq 1\,\mathrm{GeV}$: $\mathbf{Q}(x) = Q_\gamma + \beta \cdot H_{\mathrm{TKR}} + x \cdot q_7$.
  - For $E_\gamma > 1\,\mathrm{GeV}$: $\mathbf{Q}(x) = Q_\gamma + x \cdot q_7$.

The observables are efficient when a minimum is apparent in their corresponding curve. When dotted and solid lines meet, one of the iteration returns $\alpha = 0$ or $\beta = 0$. For instance, no variance reduction is observed using H_{TKR} above 30 GeV and using q_7 below 30 GeV. This is not so at 30 GeV.

3.3 Defining the X_L PDF

Once the optimization has been carried out, precise X_L distributions can be calculated for discrete Monte-Carlo energies. These distributions can be normalised to the number of entries and characterized using lognormal functions. This done, the PDFs are completely defined by the following tabulated parameters:

- Occupancy (C_{Pop}): percentage of events making the PDF class amongs all Monte-Carlo events with a TKR trigger and reconstructed direction.
- β and α, defining X_L.
- Lognormal parameters: norm (N), MPV (μ), width (σ), tail (τ) parameters.

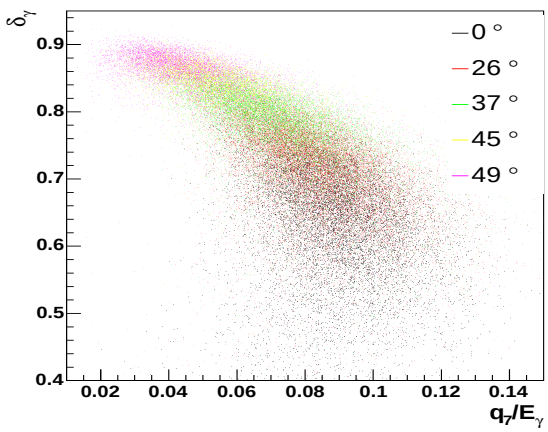

Figure 20: δ_γ versus q_7 for $E_\gamma = 10\,\mathrm{GeV}$ and $D_{\mathrm{cracks}} > 100\,\mathrm{mm}$, at different angles from the vertical.

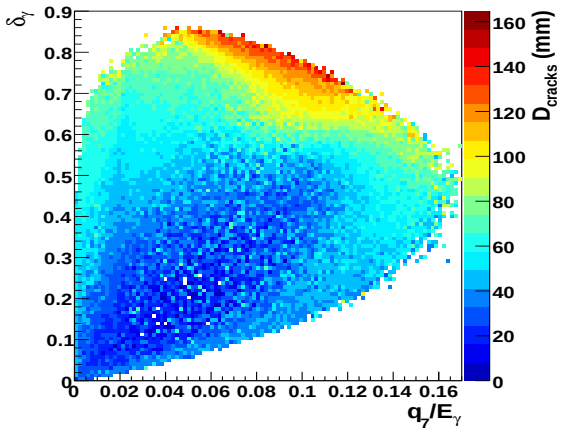

Figure 21: δ_γ versus q_7 for $E_\gamma = 100\,\mathrm{GeV}$, $\theta = 45\,°$. The color bar indicates the mean D_{cracks} value. The correlation between Q_γ and q_7 varying from positive to negative values, can be characterized using D_{cracks}.

The lognormal is defined in appendix D:

Previously, the weights were estimated with respect to E_γ and $\cos\theta$ and their behavior parametrised using a single function (see [8], appendix A). Rather than finding different functions to globally parametrise each and every parameter in the table, it was thought simpler to estimate the PDFs in between calculated E_γ values using a linear interpolation of the tables. As will be seen in section 4, this interpolation is in fact 2-dimensional, running on tables calculated at discrete E_γ and $\cos\theta$ values. The PDFs are estimated as $C_{Pop} \cdot \mathrm{logN}(X_L)$, with all parameters in the tables depending on $\tilde{E}_\gamma$ and $\cos\tilde{\theta}$ (reconstructed values for E_γ and $\cos\theta$): the interpolations is performed for these reconstruction values.

4 Defining Classes of Events

Photons may impact on the LAT from any direction. Yet as shown on Fig. 20 for 10 GeV photons, the correlations may vary greatly with the incoming angle. Cracks in between the LAT towers add another challenge in the correct calculation of the correlations. Fig. 21 shows how this correlation is affected by D_{cracks}. In order to deal with this large phase-space, classes of events are created. For each of them, weights are optimized as explained in section 3.2. These classes should be defined using different parameters for the longitudinal and the lateral shower development (see section 2). Such parameters are described in subsections 4.1 and 4.2 respectively. The results are summarized in subsection 4.3.

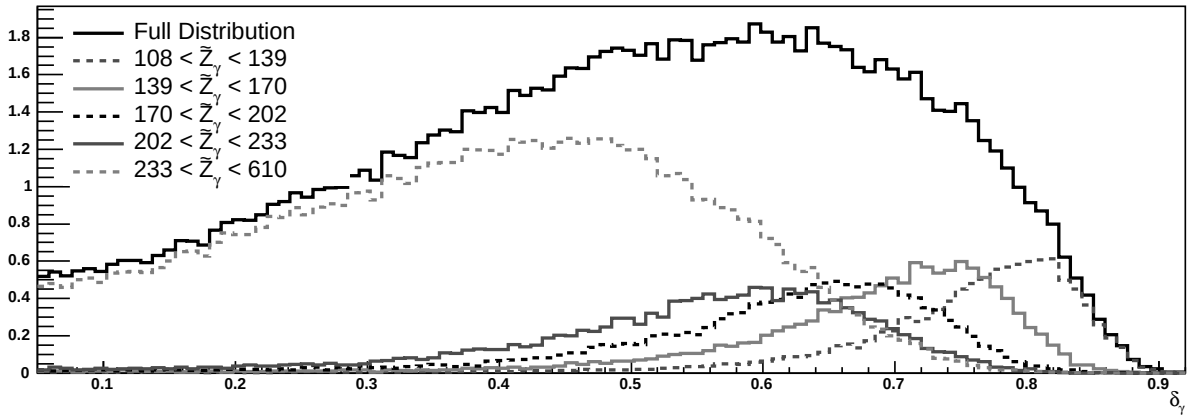

Figure 22: δ_γ for various $\tilde{Z}_\gamma$ ranges, for $E_\gamma = 100\,\mathrm{MeV}$, $\theta = 0\,^\circ$ and $D_{\mathrm{cracks}} > 120\,\mathrm{mm}$. The Q_γ distributions' MPV and shape vary with $\tilde{Z}_\gamma$, thus the latter can be used for variance reduction

4.1 Longitudinal Shower Parameters

The main longitudinal parameter is the axis along which the shower develops. This is simply the photon direction. The present method does not reconstruct this variable. Rather it relies on the reconstrution performed by the TKR. It is taken into account by running the optimizations at discrete angles to the vertical. θ is not used to define the different classes: as previously mentioned, one PDF is created per class, and, just as for E_γ, the PDF is made dependent upon the angle through an interpolation. Yet θ alone is insufficient to completly describe the mean longitudinal profile.

The mean longitudinal profile of a shower may be described using a gamma function [5]. When the depth is measured in units of radiation length, the two parameters of that function depend only on E_γ(The radiation lengths itself depends solely on the atomic composition of the detector [6]). This means that for given E_γ-fixing the shower shape- and θ -fixing the shower axis- the longitudinal sampling of the shower is fully described using the starting point of the shower. In other words, it will fully characterize the energy lost up- and dowstream of the CAL. This in turn means that the α and β parameters will also be affected by $\tilde{Z}_\gamma$. To take this into account, the method uses the reconstructed primary vertex's height $\tilde{Z}_\gamma$. Fig. 22 shows the strong dependance of energy distributions in the CAL, affecting both MPVs and spreads, depending on $\tilde{Z}_\gamma$ for a given photon energy and direction. Close to the CAL, little energy is lost to the TKR and the distribution has both a higher MPV and lower spread than for higher vertexes.

The variance reduction, using this observable, could be performed in a manner similar to the one for q_7 and H_{TKR}: adding $\gamma \cdot \tilde{Z}_\gamma$ to equation 5. Yet this would not take into account the α and β dependency in $\tilde{Z}_\gamma$. In order to do so the latter weights are rather independently optimized for each and every H_{TKR}value. Since the TKR is composed of planes of Si strips, the latter observable sports roughly discrete values.

As should be expected, for a fixed photon energy E_γ, H_{TKR} increases with $\tilde{Z}_\gamma$. Yet H_{TKR} can still be used for variance reduction. In other words, although the mean H_{TKR}

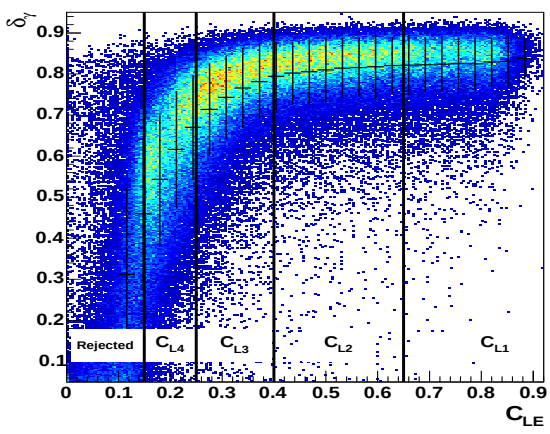

Figure 23: CAL total energy deposition versus C_{LE}, for $E_\gamma = 1\,\mathrm{GeV}$, $\theta = 32°$. Errors in black show the RMS of the Q_γ distribution.

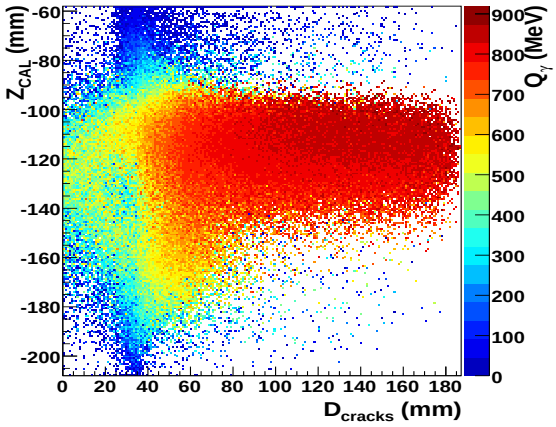

Figure 24: CAL energy centroid height versus it's distance to the tower edge, for $E_\gamma = 1\,\mathrm{GeV}$, $\theta = 32°$. The color bar shows the mean energy deposit in the CAL.

value increases with $\tilde{Z}_\gamma$, at a given vertex altitude there are still some fluctuations in shower development, thus energy deposition fluctuations in the TKR. These are positively correlated to H_{TKR} and justify its use in equation 5. In fact, Fig. 5 showing H_{TKR} versus Q_γ was created for $\tilde{Z}_\gamma \sim 420\,\mathrm{mm}$. Fig. 5 showing q_7 versus Q_γ was created for $\tilde{Z}_\gamma \sim 110\,\mathrm{mm}$.

4.2 Lateral Shower Parameters

Considering on-axis photons, as shown in Fig. 2, two regimes are possible. At lower energies, the only leaks from the CAL occur through the sides of the towers. At higher energies, leaks through the bottom of the CAL also occur. Yet, at high incidence, the situation remains similar because lateral leaks need only lateral shower parameters to describe them; and much the same is true for longitudinal leaks. The problem becomes complex for off-axis photons. Then both longitudinal and lateral leaks should be described using both longitudinal and lateral shower parameters.

Low Energies: $\tilde{\mathbf{E}}_\gamma < 3\,\mathbf{GeV}$. Dealing with lateral leaks requires some sort of knowledge of the lateral energy profile. As pointed out such information is scarce if not non-existent at lower energies. For this reason, the lateral leaks are estimated relying completely on the position and direction reconstructed by the tracker. The parameter used is the sum of the lateral distance of the track to the tower edge, weighted by the energy in the present layer:

$$C_{LE} = \frac{\int_{path} distance(tower\ gap) \cdot q_i}{Q_\gamma \cdot pathlength} \tag{6}$$

A normalisation factor is applied so that the parameter ranges between 0 and 1. This parameter is somewhat similar to the parameter D_{cracks} described further down, yet correlating

in a more straightforward fashion with the Q_γ distribution widths. Fig. 23 shows the Q_γ distribution versus this parameter. Cuts are defined on this parameter which depend neither on E_γ nor on $\cos\theta$. The ranges are, in decreasing order of quality:

- C_{L1}: $C_{LE} > .65$: best.
- C_{L2}: $.4 < C_{LE} < .65$
- C_{L3}: $.25 < C_{LE} < .4$
- C_{L4}: $.15 < C_{LE} < .25$: worse.
- C_{L5}: $C_{LE} < .15$: rejected.

High Energies, High Incidence: $\tilde{\mathbf{E}}_\gamma > 700\,\mathbf{MeV}$ and $\tilde{\theta} > 18^\circ$. In this regime the energy leaking through the bottom of the CAL should not be ignored. Yet lateral leaks will affect the shower development. For this reason finer cuts are produced using the two parameters describing the energy centroid in the CAL:

- $D_{\rm cracks}$: the centroid's lateral distance to the tower edge.
- $Z_{\rm CAL}$: height of the centroid in the CAL.

Fig. 24 shows the distribution for the two parameters. The color code shows the mean energy deposit in the CAL as a function of the two. Using these, different event populations can be considered. They are displayed on Fig. 25 as a function of $D_{\rm cracks}$ and $Z_{\rm CAL}$:

- populations fully in the center (Pop_{core} in mauve open circles, and Pop_{shell} in blue inverted triangles): there are basically no lateral leaks. The reconstruction will distinguish between two such populations, fully and somewhat off-center, simply to improve the error estimation.
- populations off-center with a $Z_{\rm CAL}$ nearer to the bottom (Pop_{bottom} in green triangles): it corresponds to cross-towers events or those missing the first layers, and in any case with a large amount of their energy deposit in the last layer.
- populations off-center with a $Z_{\rm CAL}$ nearer to the top (Pop_{top} in red squares): it corresponds to events missing the last layers. These have very low energy deposits in the CAL, almost none in the last layer. They cannot be reconstructed well using the present method.
- any event left out from these populations is rejected ($Pop_{rejected}$ in black filled circles).

q_7 is also used to fully distinguish these populations, as visible on Fig. 28.

The main point in this division of the phase-space is the separation of sets of events with comparable behavior for Q_γ and q_7. Fig. 26 shows how these cuts divide the Q_γ versus q_7

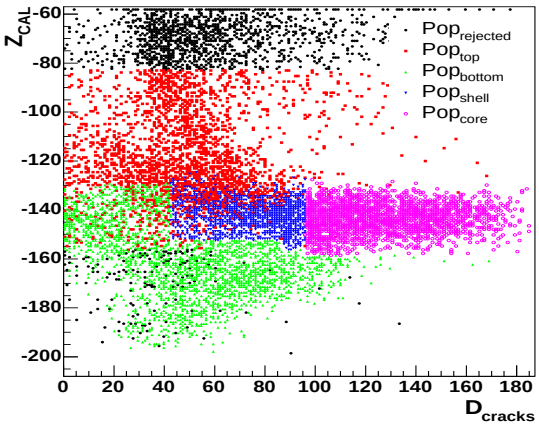

Figure 25: CAL energy centroid height versus its distance to the tower edge, for $E_\gamma = 100\,\mathrm{GeV}$, $\theta = 45\,^\circ$.

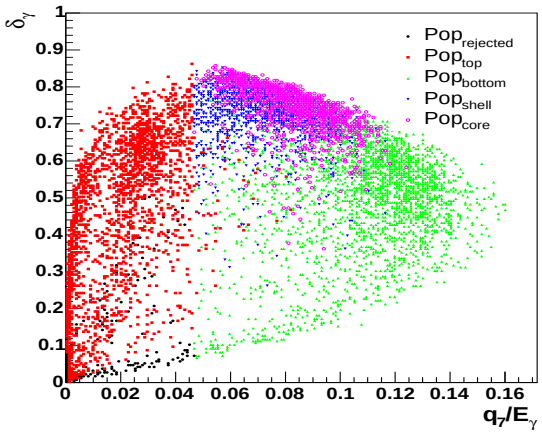

Figure 26: CAL total energy deposit versus that in the last layer, for $E_\gamma = 100\,\mathrm{GeV}$, $\theta = 45\,^\circ$.

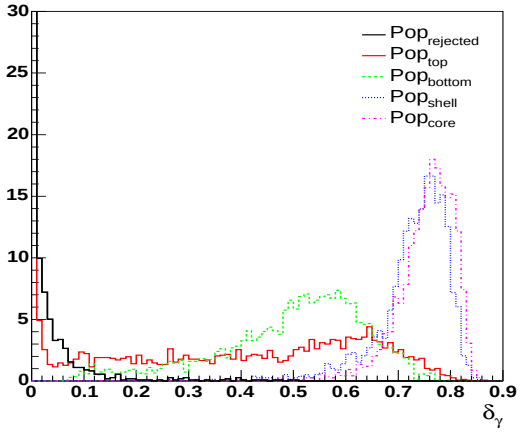

Figure 27: Q_γ for $E_\gamma = 100\,\mathrm{GeV}$, $\theta = 45\,^\circ$. Cuts on D_{cracks} and Z_{CAL} clearly distinguish between different Q_γ distributions.

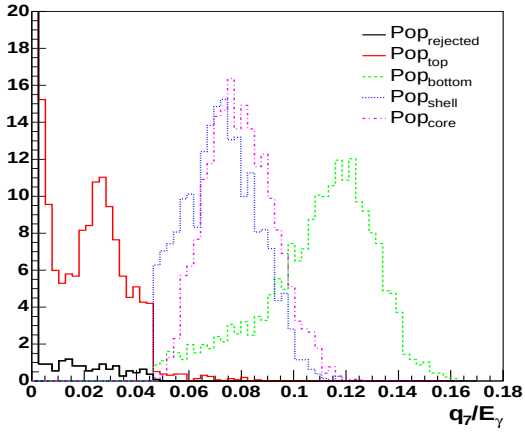

Figure 28: q_7 for $E_\gamma = 100\,\mathrm{GeV}$, $\theta = 45\,^\circ$. Cuts on D_{cracks} and Z_{CAL} clearly distinguish between different q_7 distributions.

space. The Q_γ and q_7 distributions are displayed independently on Fig. 27 and 28. These two distributions show that the classes are efficient in distinguishing these populations. This has a direct impact on the method's resolution.

The calibration of these populations is done by characterizing distributions for q_7, Z_{CAL} and D_{cracks} using the lognormal function. The class cut on these parameters are then estimated as a distance to their most probable value. This distance is calculated using the lognormal's cumulative distribution and thus taking into account the distributions'asymetry. The exact algorithm to determine the populations was defined through extensive trial and error on a wide range of E_γ and $\cos\theta$ values. Cuts were found that:

1. isolated the best events, Pop_{core} and Pop_{shell}.
2. separated the remaining events homogeneously as regarding the q_7 distributions.

For information, the distributions and the cuts they yield are:

- The Z_{CAL} and q_7 distributions for events in the center of the tower, yielding all cuts on these parameters.
- The D_{cracks} distribution for events with low Z_{CAL}, yielding a D_{cracks} cut value between Pop_{core} and Pop_{shell}. This demarquation line is visible on Fig. 25.
- The D_{cracks} distribution for events with high energy deposit with Z_{CAL} in the Pop_{shell} range, yielding a D_{cracks} cut value between Pop_{shell} and Pop_{bottom} as well as Pop_{shell} and Pop_{top}.
- The D_{cracks} distribution for events with low energy deposit with Z_{CAL} ouside the Pop_{shell} range, yielding a D_{cracks} cut value between Pop_{shell} and Pop_{bottom} or Pop_{top}, closer to the tower edge.

High Energies, Low Incidence: $\tilde{\mathbf{E}}_\gamma > 700\,\mathbf{MeV}$ and $\tilde{\theta} < 26\,^\circ$. At low incidence, the Z_{CAL} parameter becomes meaningless regarding lateral leaks whereas the D_{cracks} tends towards the C_{LE} parameter. For this reason, above 1.5 GeV, the reconstruction will use either sets of parameters depending on the energy:

- $\theta < 26\,^\circ$: use C_{LE}.
- $\theta > 18\,^\circ$: use D_{cracks}, Z_{CAL}, q_7.

4.3 Class Definition Conclusion

Classes can be regrouped hierarchically into:

1. 3 major sets, depending on the photon values for E_γ and $\cos\theta$.

- Low energy: $< 3\,\mathrm{GeV}$. It uses the lateral parameter C_{LE}.
- High energy, low incidence: $\tilde{E}_\gamma > 1.5\,\mathrm{GeV}$, $\tilde{\theta} < 26\,^\circ$, using C_{LE}
- High energy, high incidence: $\tilde{E}_\gamma > 700\,\mathrm{MeV}$, $\tilde{\theta} > 18\,^\circ$, using D_{cracks} and Z_{CAL} and q_7.

2. 4 subsets defined using the major sets' respective lateral parameters.

3. 1 set of 16 classes, depending on the value of $\tilde{Z}_\gamma$

This hierarchy is reflected in GlastRelease code, starting in the second installment of the CalLikelihoodTool in the CalRecon package (Not yet committed at the percent time).

For each and every one of these classes, a PDF is created. In principle, it should be possible to calculate one single PDF which would depend not only on E_γ and $\cos\theta$ but also on the other shower parameters mentioned in this section. In practice, this would require running the optimization on a very fine shower parameter grid. In other words it would necessitate considerable amounts of simulated events. The corollary of this is that, as we have a coarse grid - only 4 different classes - the PDFs are somewhat imprecise. This is why, in the reconstruction, they will be considered independently. This will particularly affect the efficiency of the error parameter returned by the reconstruction.

On their overlap "low energy" and "high energy, low incidence" have rigorously the same PDFs. As such, they return the same result. This is necessary because PDFs are defined for a given range, $[E_\gamma^{Min}, E_\gamma^{Max}]$, and an error estimation cannot be carried out when $\tilde{E}_\gamma$ is too close to either E_γ^{Min} or E_γ^{Max}.

5 The Reconstruction

The reconstruction is based on a maximum likelihood, using the PDFs as defined in paragraphs 3.2 and 4. The principles for the maximum likelihood are discussed in section 5.1 as well as its advantages compared to the method used previous in the previous last layer tool. Subsection 5.2 illustrates the reconstruction for 1 event. Finally the performance of the reconstruction is explored in subsection 5.3.

5.1 The Maximum-Likelihood Principles

The method described here relies on the probability density function of one GLAST observable. The idea is to make extensive use of the GLAST detector simulation to accurately describe the PDF. The simulation includes both the physics, relying on the GEANT4 simulator, and the off-line reconstruction algorithms. The advantage of such a method is to factor in awkward detector effects which cannot easily be described in an analytic fashion. These range from a detector geometry, at odds with that of the electromagnetic showers it measures, to systematics in the detector calibration or TKR reconstruction. Another advantage is that such a method can be made to rely on the shape of observable distributions rather than their

mean value. Mainly, correlations are made not between mean values but between their most probable value, with an implicit correction for distribution asymetries. This depends on the method providing the calibration of the function, discussed in section 3.2.

The PDFs for the present reconstruction methods are given by the distributions of the observable X_L, defined in equation 1. Each distribution is the probability distribution of the X_L, for photons with a given energy and angle to the vertical, inside a defined section Pop_χ of the GLAST phase-space, corresponding to a particular class of events; χ can either be *top*, *bottom*, *shell* or *core*. These distributions are weighted by the ratio of events making the class cuts to those that don't, at a specific E_γ. Thus they are the product of two probabilities:

$$PDF() = P(X_L \mid event \in Pop_\chi) P(event \in Pop_\chi \mid E_\gamma \,\&\&\, \cos\theta) \tag{7}$$

We assume that the product becomes:

$$PDF() = P(X_L \mid event \in Pop_\chi \,\&\&\, E_\gamma \,\&\&\, \cos\theta) \tag{8}$$

Using these, we may then calculate the probability:

$$P(\tilde{E}_\gamma \mid \cos\tilde{\theta} \,\&\&\, X_L \,\&\&\, event \in Pop_\chi) \tag{9}$$

The parametrisation of the PDFs is explained in section 3.3. The reconstructed energy for one PDF is the one maximising that probability. As, in the reconstruction, the photon energy is the only free parameter of the probability, finding the maximum is a simple process. An error can be estimated by returning the full-width-half-maximum (FWHM) of the distribution PDF($\tilde{E}_\gamma$). This information is an effective quality indicator of this reconstruction, as will be shown in subsection 5.3.

The advantages of this method are twofold compared to the previous one. The latter was a simple recursive estimation:

$$\tilde{E}^0_\gamma = Q_\gamma + \alpha(Q_\gamma) \cdot q_7 \tag{10}$$

$$\tilde{E}^n_\gamma = Q_\gamma + \alpha(\tilde{E}^{n-1}_\gamma) \cdot q_7 \tag{11}$$

Two iterations at least were necessary. Although such a method reduces the bias, it does so at the expense of the resolution. Also, it cannot provide with an error as the maximum likelihood can. An additionnal bonus of the maximum likelihood is, as shown previously, the possibility of choosing the best solution between different classes.

5.2 Event reconstruction

As seen in section 4, a great number of PDFs are constructed, each of them for a different section of the LAT phase-space. It was not deemed possible to create one global PDF from all of these because of the coarse graining of the phase-space the classes represent. Yet the class cuts were shown to vary depending on the photon energy, that which we are looking for. This means that an event may qualify for a number of PDFs. The selection criteria are the following :

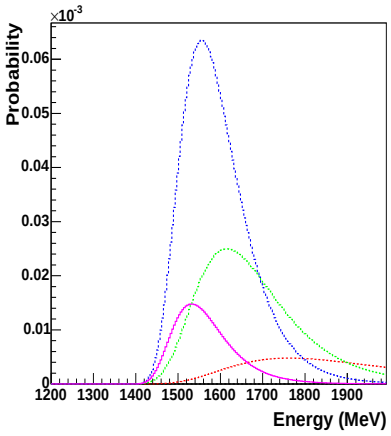

Figure 29: PDFs from the "low energy" major class set.

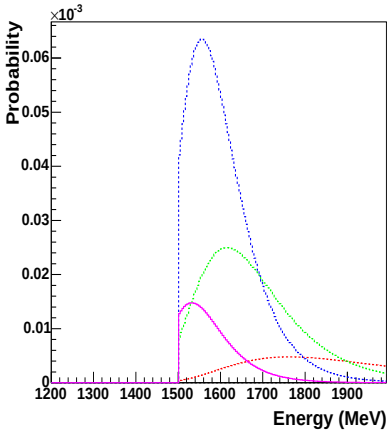

Figure 30: PDFs from the "high energy, low incidence" major class set.

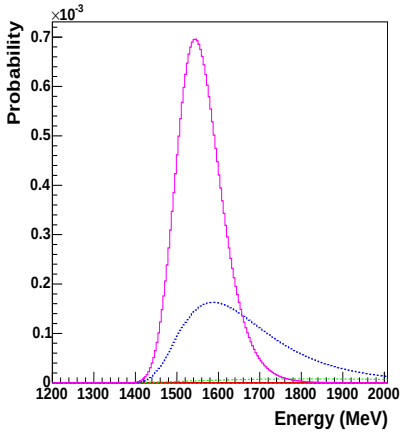

Figure 31: PDFs from the "high energy, high incidence" major class set.

1. PDFs are created for a certain $\tilde{Z}_\gamma$ range each. When the event $\tilde{Z}_\gamma$value sits outside the range, the PDF is rejected.
2. idem for the $\cos\tilde{\theta}$ range.
3. PDFs are defined for a certain E_γ range. PDFs may be rejected for Q_γ too far below or higher than that range.
4. After calculations, PDFs may return an energy estimation below $Q_\gamma$for that event. In such a case, the PDF is rejected.

Calculations are carried out for each PDF. Verifications are made that the PDFs from the "hight energy, low incidence" major set pass the cuts on Z_{CAL} and D_{cracks} which depend on the energy they return. The PDF having the highest probability amongst those passing all their cuts is returned. It may happen that only PDFs from the "hight energy, low incidence" major set qualifies, yet none of these return an energy for which Z_{CAL} and D_{cracks} pass the corresponding cuts. In this case, the PDF with the highest probability is still returned.

Let us consider a photon with parameters:

- $E_\gamma = 1.5\,\mathrm{GeV}$
- $\theta = \tilde{\theta} = 24\,^\circ$
- $\tilde{Z}_\gamma = 420.\,\mathrm{mm}$ (this is a thin tray).
- $Q_\gamma = 1.2\,\mathrm{GeV} = 0.8 * E_\gamma$
- $q_7 = .09\,\mathrm{GeV} = 0.06 * E_\gamma$
- $H_{\mathrm{TKR}} = 148$

- $Z_{\mathrm{CAL}} = -128\,\mathrm{mm}$
- $D_{\mathrm{cracks}} = 140\,\mathrm{mm}$
- $C_{LE} = 0.8$

Such a photon would qualify for all 3 major sets, 192 PDFs, described in section 4.3. From among these PDFs, only 12 qualify for the $\tilde{Z}_\gamma = 420\,\mathrm{mm}$ criterium. They are reported in Fig. 31, 29 and 30, for the "high energy, low incidence", "low energy" and "high energy, high incidence" major sets respectively (Note that the y-axis range is different). On each of these are the PDFs for all subsets. The color coding is the one given for the different populations in section 4.2. From best to worst, we have:

- in mauve: Pop_{core} for Fig. 31, C_{L1} for Fig. 29 and 30.
- in blue: Pop_{shell} for Fig. 31, C_{L2} for Fig. 29 and 30.
- in green: Pop_{bottom} for Fig. 31, C_{L3} for Fig. 29 and 30.
- in red: Pop_{bottom} for Fig. 31, C_{L4} for Fig. 29 and 30.

Dotted lines show those PDFs for which the cuts on either C_{LE} or Z_{CAL} and D_{cracks} are not met. Thus only the mauve PDFs qualify for the final selection (Only one line is in theory calculated for major sets represented on Fig. 29 and 30. The dotted lines are only here for illustration purposes). The reconstruted value is the MPV with the highest peak: this is the mauve population for Fig. 31. The reconstructed energy is 1.544 GeV. Fig. 30 and Fig. 29 are similar since they are produced with rigorously the same classes and tables on their energy range overlap, as pointed out in 4.3. The PDFs on Fig. 30 are not defined for energies below 1.5 GeV, and therefore the corresponding curves are cut off at that energy.

Once a PDF has been chosen, an error estimation, its FWHM, can also be returned. In this case the FWHM from the mauve curve on Fig. 31 is returned: 4.1%. As a PDF is defined on an energy range: $[E_\gamma^{Min}, E_\gamma^{Max}]$, we must have both min and max FWHM values inside that range for an estimation to be carried out. It may happen that one of the values is not found. In this case, the curve selected by the reconstruction would have been truncated on either the low or the high energy side, as in Fig. 30, but never both; this is simply because the PDF energy range is sufficiently large. When only either the max or the min is inside the range, an estimation on the other one is still carried out. It is based on the idea that there is a sub-range $[E_\gamma^{MinII}, E_\gamma^{MaxII}] \subset [E_\gamma^{Min}, E_\gamma^{Max}]$ for which the FWHM is always defined. The trick is then to find the value Q_γ^{New} closest to its true value Q_γ such that, without changing any other observable, the corresponding reconstructed energy be inside that sub-range: $\tilde{E}_\gamma^{New} \in [E_\gamma^{MinII}, E_\gamma^{MaxII}]$. The missing half of the FWHM range is estimated for the value Q_γ^{New}.

5.3 Performance

Results are described separately for photons with their primary reconstructed vertexes in the thin or thick strips. On axis, they represent respectively 60 and 40% of TKR recontructed

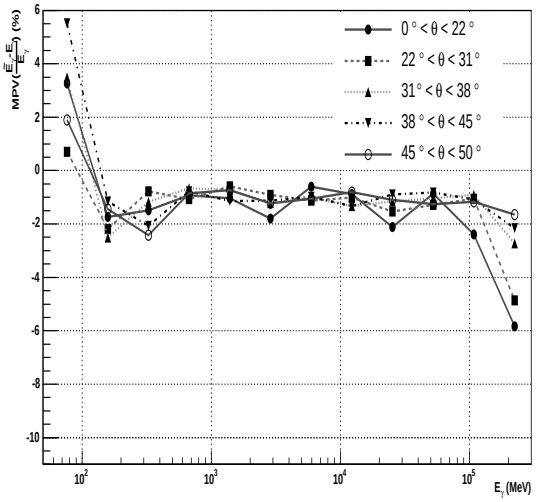

Figure 32: Bias for thin strips.

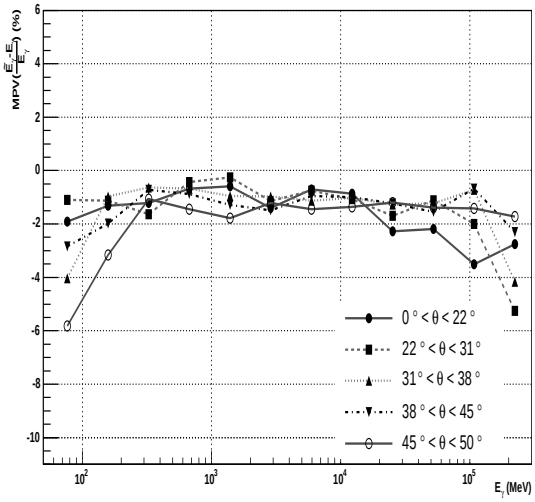

Figure 33: Bias for thick strips.

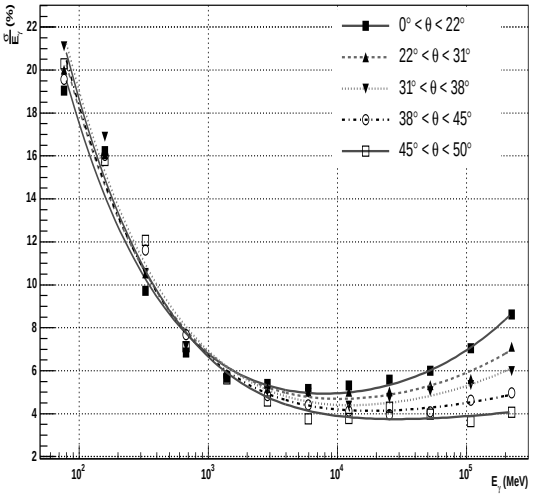

Figure 34: Resolution for thin strips.

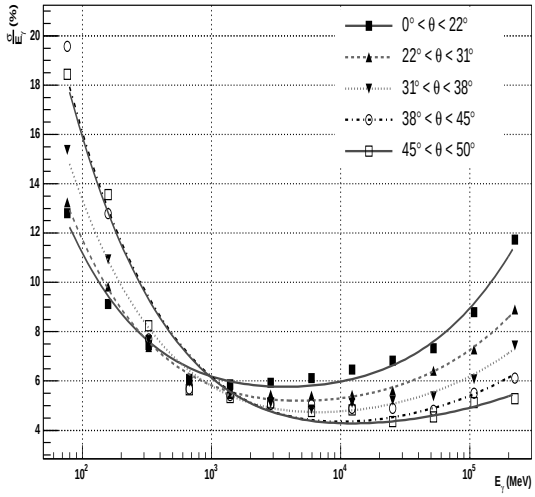

Figure 35: Resolution for thick strips.

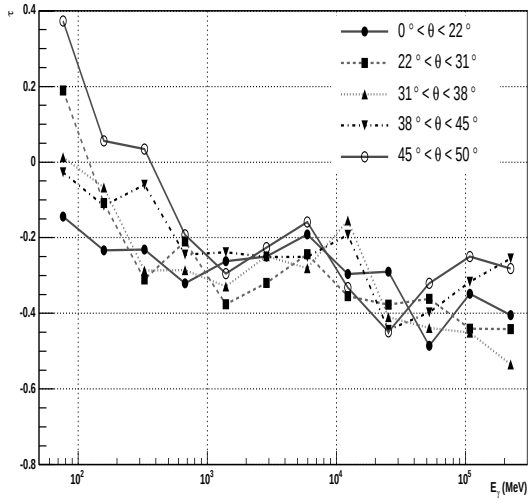

Figure 36: Tail for thin strips.

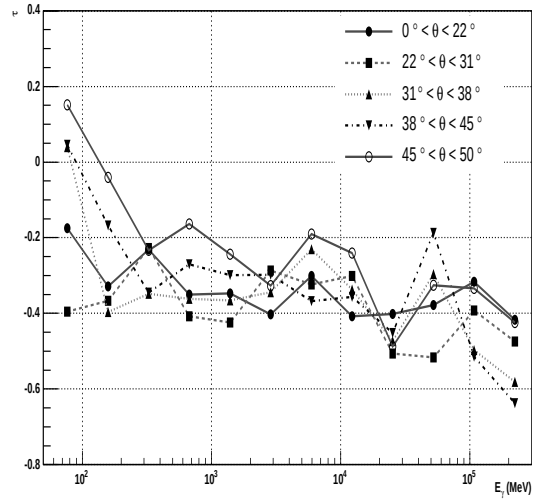

Figure 37: Tail for thick strips.

	$a\,(\mathrm{GeV})$	b	c
$0\,^\circ < \theta < 22\,^\circ$	5.40 ± 0.21	3.99 ± 0.55	0.75 ± 0.05
$22\,^\circ < \theta < 31\,^\circ$	5.62 ± 0.16	3.79 ± 0.43	0.65 ± 0.05
$31\,^\circ < \theta < 38\,^\circ$	5.92 ± 0.17	3.46 ± 0.49	0.60 ± 0.07
$38\,^\circ < \theta < 45\,^\circ$	5.70 ± 0.17	3.38 ± 0.52	0.46 ± 0.12
$45\,^\circ < \theta < 50\,^\circ$	5.81 ± 0.17	3.08 ± 0.57	0.36 ± 0.19

Table 1: Resolution parameters for the thin strips.

	$a\,(\mathrm{GeV})$	b	c
$0\,^\circ < \theta < 22\,^\circ$	3.12 ± 0.10	5.25 ± 0.17	0.86 ± 0.01
$22\,^\circ < \theta < 31\,^\circ$	3.41 ± 0.04	4.62 ± 0.08	0.75 ± 0.01
$31\,^\circ < \theta < 38\,^\circ$	4.02 ± 0.08	4.06 ± 0.17	0.67 ± 0.02
$38\,^\circ < \theta < 45\,^\circ$	4.97 ± 0.22	3.52 ± 0.58	0.61 ± 0.08
$45\,^\circ < \theta < 50\,^\circ$	4.90 ± 0.17	3.55 ± 0.45	0.53 ± 0.09

Table 2: Resolution parameters for the thick strips.

events. The cuts applied are $Q_\gamma > 10\,\mathrm{MeV}$. The events are generated using GlastRelease v7r2 for an all gamma source. Energies range from 20 MeV to 300 GeV. The figures discussed next show the resolution, bias and tail parameters as a function of Monte-Carlo energy on the x-axis and the angle to the vertical on the y-axis.

Bias, Resolution and Tails: The method's resolution is shown on Fig. 34 and Fig. 35. The resolutions are defined as the lognormal width σ (see equation 14), with the lognormal fitted to the $\frac{\tilde{E}_\gamma}{E_\gamma}$ distributions. These results are parametrised using the function :

$$\frac{\sigma(E)}{E} = \sqrt{\frac{a^2}{E} + b^2 + E^c} \tag{12}$$

These terms correspond to:

1. A stochastic term corresponding to the fluctuations in shower depth for a same photon energy.
2. A constant term related to instrumental effects, not depending on the photon energy.
3. A high energy term, resulting from the energy leaks through the bottom of the CAL.

The fit parameters and their error are reported in tables 1 and 2 for thin and thick strips respectively. The parametrisation if correct for an energy scale in GeV.

The first two terms are classic features of calorimetry resolution. The parameter a is expected to be in the 5-20% range [4]. In our case, $a \simeq 5\%$, although the last term in the equation, which is not a classic feature, does affect these values. This term is important up

the GeV range. The second term, describing instrumental effects, is also in the expected range of $b \simeq 4\%$. This term is significant for energies in the GeV range. This explains why it is greater for photons materializing in thick rather than thin strips. A third term used in reference [4] (Eq. 14) does not appear in our parametrisation. This term corresponds to noise in the photo-multipliers, photodiodes or equivalent apparatuses, and is parametrized by E^{-2} in the quadratic sum. In the case of the CAL photodiodes, it should be negligeable compared to the other terms. Including it in Eq. 12 resulted in overfitting, with akward values and errors for the amplitude of this term. It was thus discarded. The last term in Eq. 12 is not present in reference [4]. It describes energy leaks occuring through the bottom of the CAL. More often than not, earth-based calorimeters can be made thick enough that such leaks never become the dominant features in resolution. This is not the case here. We describe it here using a power law.

Results from thes figures can be summarized as follows:

- The resolution is best off-axis ($> 10\,^\circ$) and for energies beyond 1 GeV. This is where energy leaks are the least important.
- For low energy photons (< 200 MeV), the resolution is particularly poor. In this case, little or none of the shower actually reaches the CAL. For the same reason, the resolution quickly deteriorates with increasing incidence.
- For high energy photons (> 10 GeV), the resolution improves with increasing incidence. In this range, the most important leaks occur through the bottom of the CAL. They become negligeable at very high incidence. For instance, for thin tray, Pop_{core} photons around $E_\gamma = 50$ GeV, $\theta = 32\,^\circ$, the energy deposit is 88 % of the photon energy, and its variance is already as low as 3.5%. In this case, the method is effectively de-biasing the Q_γ value.

Biases are displayed in Fig. 32 and Fig. 33. They are of the order of 1%. The large amounts are due to low event counts and incorrect fits.

Lognormal tail parameters visible in Fig. 36 and Fig. 37 are negative, mostly around -0.4, meaning that the dominant tail in the reconstruction is toward the low energies.

Error Estimator: The PDF FWHM, normalised to the reconstructed energy, is returned as an error estimation. Fig. 38 shows how it correlates with the resolution. On the y-axis is the distance to the Monte-Carlo truth in %. On the bottom axis is the error estimation. Black error bars indicate the mean bias and the spread of the distribution. The spreads are reported in Fig. 39 as a function of the error estimation. Dominant low-energy tails in the reconstruction result in the mean biases on Fig. 38 being negative. The different classes of events are visible as agglomerations on the graph. This means that the error estimation is strongly dependant on the class of events. Thus, the efficiency of this parameter relies heavily on a correct calibration of the different class parameters.

This error estimation is not a 68% confidence interval, the error estimation normaly assiciated to a maximum likelihood. It has in fact no true statistical meaning. Nonetheless,

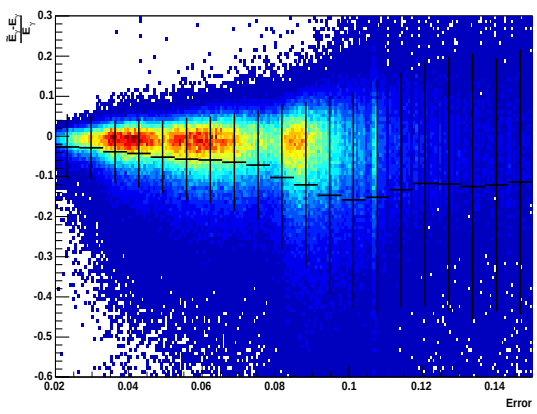

Figure 38: Distance to the Monte-Carlo truth energy versus the error estimation.

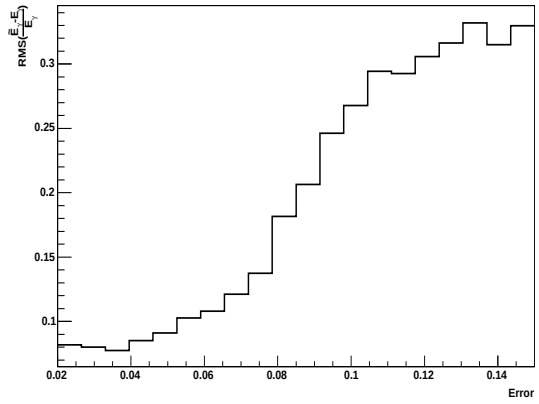

Figure 39: RMS of the distributions: distance to the Monte-Carlo truth energy, as a function of the error estimaton.

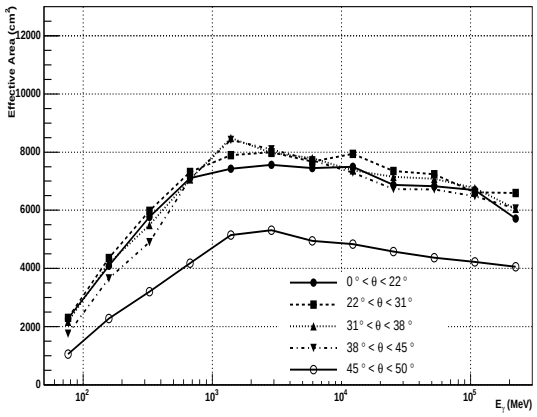

Figure 40: Effective area as a function of energy for $|\frac{\tilde{E}_\gamma - E_\gamma}{E_\gamma}| < .1$.

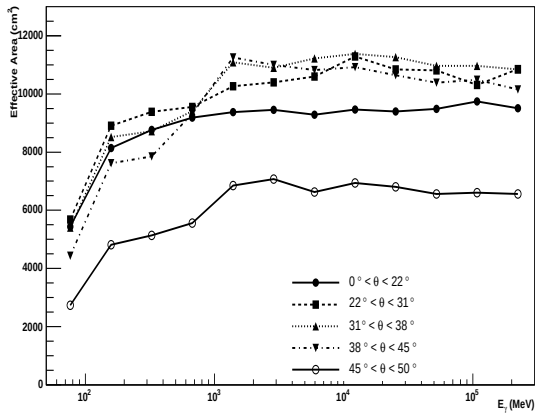

Figure 41: Effective area as a function of energy for $|\frac{\tilde{E}_\gamma - E_\gamma}{E_\gamma}| < .5$.

Fig. 39 shows that it may still be relevent for dertermining the quality of an event. In theory, it should be possible to determine a 68% confidence interval. Yet technical difficulties occcur because the PDFs are only known on a certain range. This is the reason for returning the FWHM.

Effective Area: The procedure for estimating the effective area (Aeff) is explained in appendix C. In short, the LAT horizontal area is cut up in tiles. Aeff is the sum of the tiles'area weighted by the ratio of "good" to all events in the tile. Good events are defined as the ones passing all of the following cuts:

- Onboard filter status is nill, i.e. event was not rejected.
- At least one reconstructed track in the TKR.

- $Q_\gamma > 10\,\mathrm{MeV}$.
- $|\frac{\tilde{E}_\gamma - E_\gamma}{E_\gamma}| < \delta$. The latter parameter is defined as $\delta = 0.1$ on Fig. 40, $\delta = 0.5$ on Fig. 41.

The fall in efficiency for $\theta > 45^\circ$ is due to limited range in which this method is valid. It otherwise follows a curve similar to the shower containment, see Fig. 2. The same interpretation is valid. At low energies $< 100\,\mathrm{MeV}$, the TKR absorbs the shower before it reaches the CAL. Around 1 GeV, the shower containment is at its highest, all the more so for higher θs, and the method has a maximum effective area. Above 1 GeV, the effective area slowly droops as the shower increasingly leaks through the bottom of the CAL. The values in themselves are below $0.8\,\mathrm{m}^2$ for $\delta = 0.1$, and $1.1\,\mathrm{m}^2$ for $\delta = 0.5$, somewhat lower than other methods. Toby Burnett suggested using the logistic function $f(x) = \frac{a}{1+b\exp(-cx)}$ to describe the effective areas [3]. This does not seem indicated here as the droop at higher energies is much more pronounced for this method.

For the sake of comparison, similar figures are drawn for the two other calorimeter based reconstruction methods present in the ground software as of GlastRelease v7r2. These are shown in appendixes A and B (It must be emphasized that not cuts on the quality of the events are applied).

6 Conclusions

The present note describes the tranformation applied to the the last layer method. An extension of the variance reduction to low energies was performed using H_{TKR}. An extension to lower angles was also possible by distinguishing various populations using C_{LE} for lower energies ($E_\gamma < 3\,\mathrm{GeV}$) or Z_{CAL} and D_{cracks} for higher ones ($E_\gamma > 0.7\,\mathrm{GeV}$). Lastly the method uses a maximum likelihood algorithm rather than the previous recursive correction. It has the advantage of returning an unbiased estimation of the energy as well as an error estimation.

The drawbacks of the method are the same as with the previous intallation. Parameters must be extensively calculated for discrete Monte-Carlo energies and angles. This means simulating millions of events is necessary to the calibrations of the method. Another point is that many of the events are not reconstructed, wether because the calibration was not done for a particular region of phase-space, or because it was deemed that the method was not reliable enough. Both these drawbacks could in principle be reduced by yet more extensive simulations and the creation of finer classes of events.

Extending the method to CAL-only events should be relatively straightforward. In theory, an extension of the method to many failure modes should also be, as their effect will automatically register through the simulation to the calibration. In practice, it will likely become necessary to define new classes of events. As mentioned in the introduction, the photon direction's azimuthal angle is not directly taken into account. Doing so will improve the reconstruction for events with their shower close to the cracks. Another extension could be to refine on the anti-correlation variables used, in particular, by correlating energies regis-

tering in crystals or towers neighbouring the cracks, as well as through equivalent observables in the TKR.

7 Aknowledgements

I would like to thank my colleagues at LLR, Phillipe Bruel and Berrie Giebels for their help in producing this reconstruction as well as patiently proof reading this note, David Chamont for your work on making the code seaworthy. Thank you to the many GLAST colleages for their help and insights on this work.

References

[1] W. Atwood. http://www-glast.slac.stanford.edu/software/anagroup/energyalgscomparison_4.pdf. Analysis group presentation, Aug. 2005.

[2] P. Bruel. http://polywww.in2p3.fr/~bruel/calfullprofile.ps. Research note, Laboratoire Leprince-Ringuet, 2005.

[3] Toby Burnett. LAT effective area and point spread function. Technical report, University of Washington, October 2005. LATDOC-AM-04356.

[4] Christian W. Fabjan and Gianotti Fabiola. Calorimetry for Particle Physis. *Reviews of Modern Physics*, 75, October 2002.

[5] G. Grindhammer and S. Peters. The Parameterized Simulation of Electromagnetic Showers in Homogeneous and Sampling Calorimeters. *ArXiv High Energy Physics - Experiment e-prints*, January 2000.

[6] H. Bichsel, D.E. Groom and S.R. Klein. *Passage of particles through matter*, volume 3, chapter 23. EDP Science, 2005.

[7] R. Terrier. http://www-glast.slac.stanford.edu/software/workshops/september00workshop/regisenergyrecon.pdf. GLAST Software Workshop, Sept. 2000.

[8] R. Terrier. *Calorimetrie et Methodes d'Analyse Spectrale en Astronomie Gamma Spatiale.* PhD thesis, Physique Corpusculaire et Cosmologie, College de France, 2002.

Appendix A: **Performance Figures for CalFullProfile.**

The CalFullProfile method, returning a value in $CalCfpEnergy$ in the $MeritTuple$, estimates the energy by fitting the shower's longitudinal energy profile in the CAL to an incomplete gamma function, which represents the mean longitudinal profile. For further details, see [2].

The method works only for events with $Q_\gamma > 1\,\mathrm{GeV}$. For this method, biases, resolutions and tail parameters are presented in that order on Fig. 44, 46 and 48 for thin strips, and on Fig. 45, 47 and 49 for thick strips. The effective area for events are shown on 42 and 43 for $|\frac{\tilde{E}_\gamma - E_\gamma}{E_\gamma}| < .1$ and $|\frac{\tilde{E}_\gamma - E_\gamma}{E_\gamma}| < .5$ respectively.

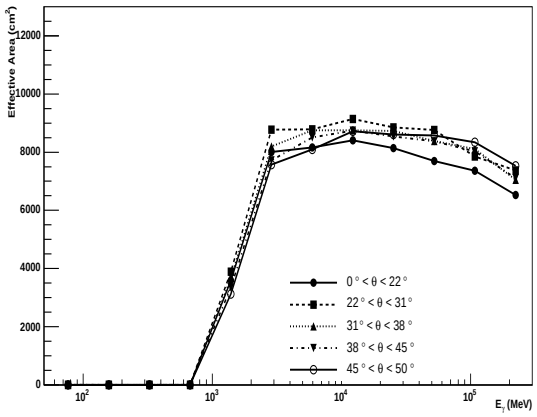

Figure 42: CalFullProfile's effective area as a function of energy for $|\frac{\tilde{E}_\gamma - E_\gamma}{E_\gamma}| < .1$.

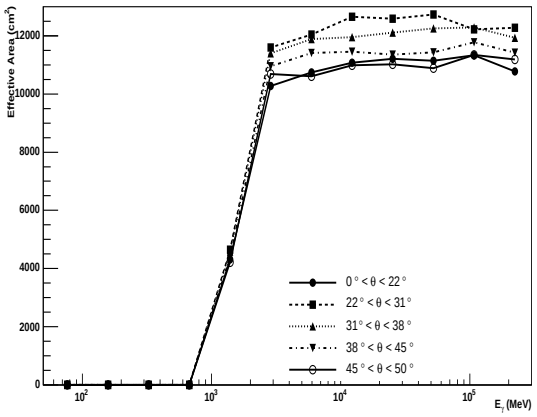

Figure 43: CalFullProfile's effective area as a function of energy for $|\frac{\tilde{E}_\gamma - E_\gamma}{E_\gamma}| < .5$.

	$a\,(\mathrm{GeV})$	b	c
$0\,^\circ < \theta < 22\,^\circ$	5.79 ± 0.60	5.32 ± 0.13	0.75 ± 0.01
$22\,^\circ < \theta < 31\,^\circ$	7.88 ± 0.69	4.65 ± 0.22	0.71 ± 0.02
$31\,^\circ < \theta < 38\,^\circ$	9.18 ± 0.50	4.23 ± 0.20	0.64 ± 0.02
$38\,^\circ < \theta < 45\,^\circ$	10.20 ± 0.26	3.67 ± 0.13	0.59 ± 0.01
$45\,^\circ < \theta < 50\,^\circ$	11.38 ± 0.29	3.12 ± 0.18	0.57 ± 0.02

Table 3: CalFullProfile's resolution parameters for the thin strips.

	$a\,(\mathrm{GeV})$	b	c
$0\,^\circ < \theta < 22\,^\circ$	3.30 ± 1.96	6.35 ± 0.21	0.84 ± 0.01
$22\,^\circ < \theta < 31\,^\circ$	5.34 ± 1.04	5.32 ± 0.21	0.81 ± 0.01
$31\,^\circ < \theta < 38\,^\circ$	7.33 ± 0.85	4.58 ± 0.26	0.74 ± 0.02
$38\,^\circ < \theta < 45\,^\circ$	7.18 ± 0.51	4.69 ± 0.15	0.60 ± 0.02
$45\,^\circ < \theta < 50\,^\circ$	7.52 ± 0.70	4.32 ± 0.23	0.58 ± 0.03

Table 4: CalFullProfile's resolution parameters for the thick strips.

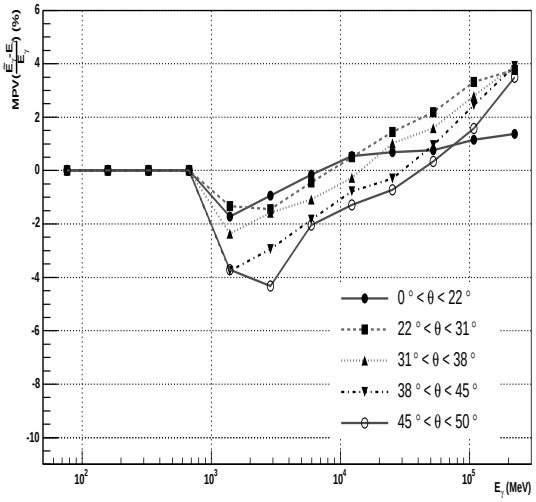

Figure 44: CalFullProfile's bias for thin strips.

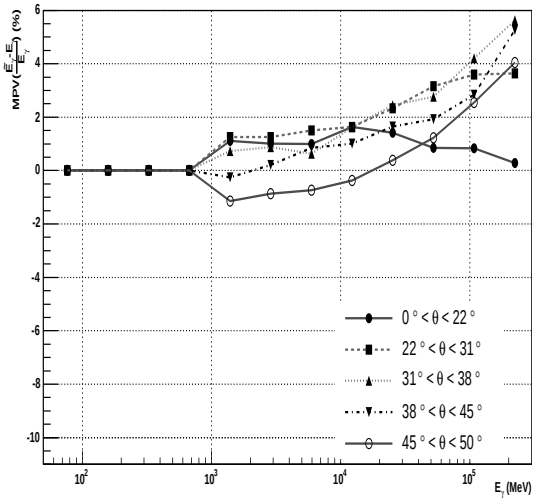

Figure 45: CalFullProfile's bias for thick strips.

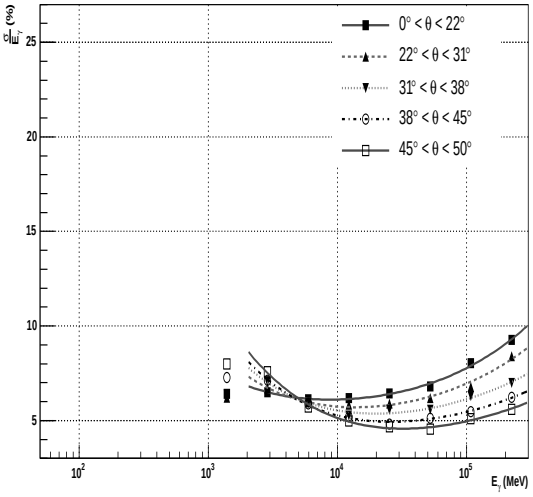

Figure 46: CalFullProfile's resolution for thin strips.

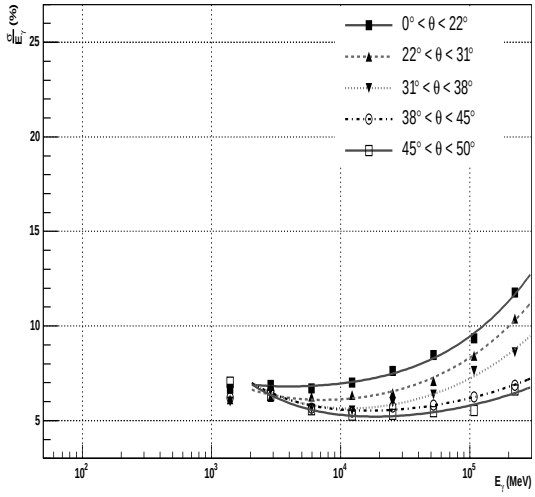

Figure 47: CalFullProfile's resolution for thick strips.

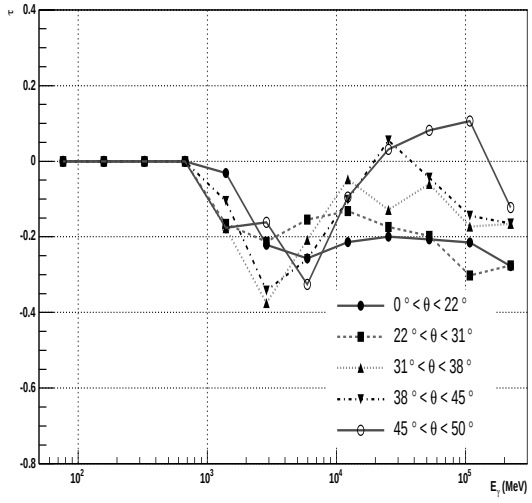

Figure 48: CalFullProfile's tail for thin strips.

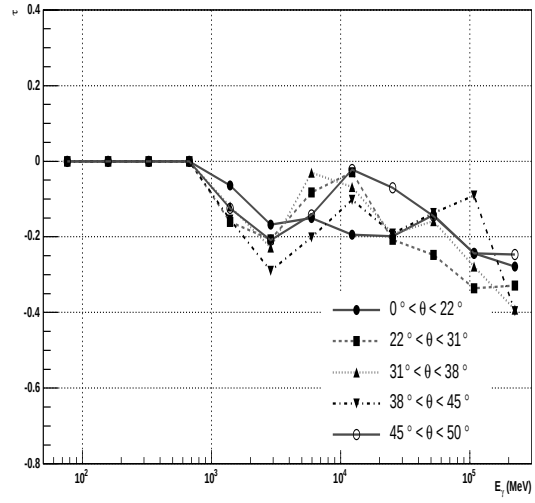

Figure 49: CalFullProfile's tail for thick strips.

Appendix B: **Performance Figures for the Parametric Method.**

The Parametric method, returning a value $EvtEnergyCorr$ in the $MeritTuple$, estimates the energy by using the relationship $T_{max} = \log(\frac{E_\gamma}{E_c})$. E_c is the critical energy and T_{max} is the depth in radiation lenght of the shower maximum. The precision and efficiency of the method relies on a correct estimation of T_{max}, thus a precise understanding of the shower propagation through the LAT's different materials in terms of mean radiation lengths.

For this method, biases, resolutions and tail parameters are presented in that order on Fig. 52, 54 and 56 for thin strips, and on Fig. 53, 55 and 57 for thick strips. The effective area for events are shown on 50 and 51 for $|\frac{\tilde{E}_\gamma - E_\gamma}{E_\gamma}| < .1$ and $|\frac{\tilde{E}_\gamma - E_\gamma}{E_\gamma}| < .5$ respectively.

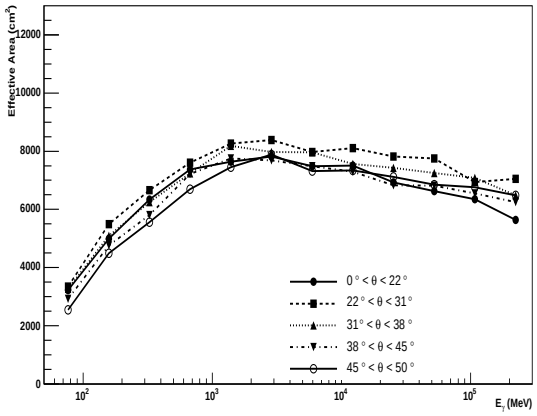

Figure 50: Parametric method's effective area as a function of energy for $|\frac{\tilde{E}_\gamma - E_\gamma}{E_\gamma}| < .1$.

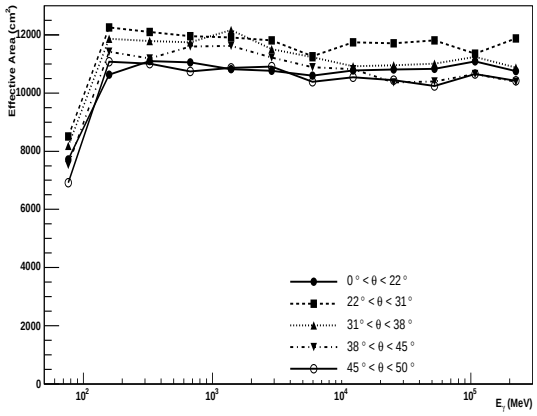

Figure 51: Parametric method's effective area as a function of energy for $|\frac{\tilde{E}_\gamma - E_\gamma}{E_\gamma}| < .5$.

	a (GeV)	b	c
$0° < \theta < 22°$	5.95 ± 0.37	5.61 ± 0.84	0.86 ± 0.06
$22° < \theta < 31°$	6.41 ± 0.23	4.30 ± 0.63	0.78 ± 0.05
$31° < \theta < 38°$	6.27 ± 0.26	4.22 ± 0.71	0.67 ± 0.09
$38° < \theta < 45°$	6.20 ± 0.29	4.49 ± 0.79	0.51 ± 0.19
$45° < \theta < 50°$	6.62 ± 0.33	4.77 ± 1.54	0.20 ± 1.89

Table 5: Parametric methods's resolution parameters for the thin strips.

	a (GeV)	b	c
$0° < \theta < 22°$	3.44 ± 0.23	6.61 ± 0.39	0.92 ± 0.03
$22° < \theta < 31°$	4.18 ± 0.17	5.04 ± 0.35	0.85 ± 0.03
$31° < \theta < 38°$	4.74 ± 0.19	4.20 ± 0.45	0.78 ± 0.04
$38° < \theta < 45°$	5.01 ± 0.07	4.40 ± 0.18	0.67 ± 0.02
$45° < \theta < 50°$	5.42 ± 0.10	4.53 ± 0.25	0.52 ± 0.06

Table 6: Parametric methods's resolution parameters for the thick strips.

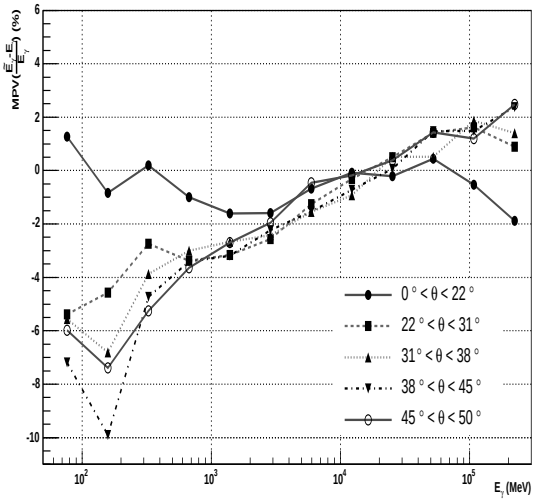

Figure 52: Parametric method's bias for thin strips.

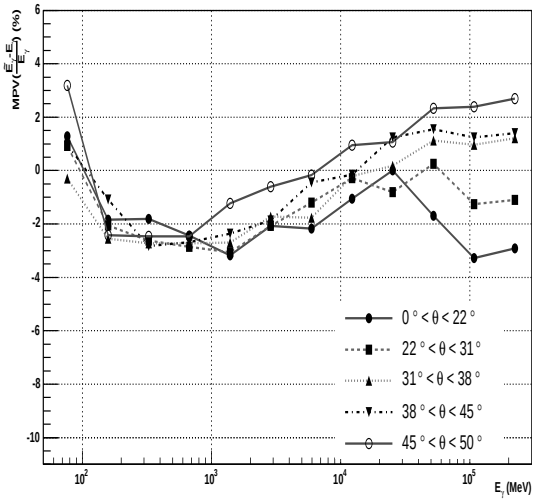

Figure 53: Parametric method's bias for thick strips.

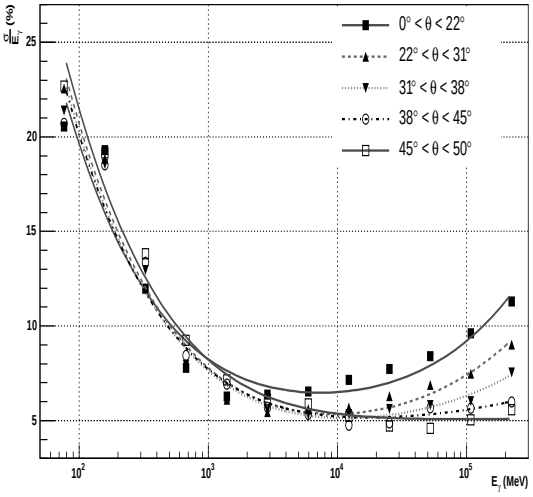

Figure 54: Parametric method's resolution for thin strips.

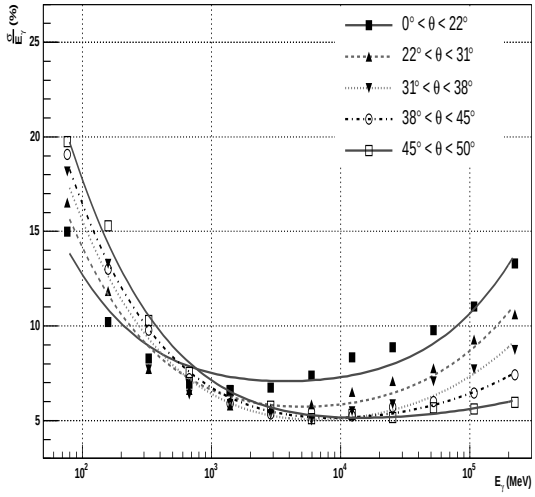

Figure 55: Parametric method's resolution for thick strips.

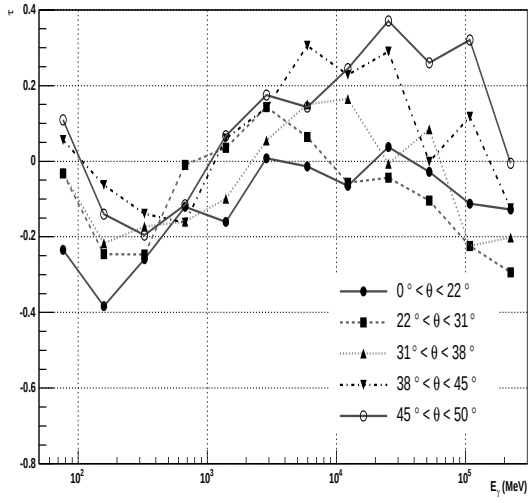

Figure 56: Parametric method's tail for thin strips.

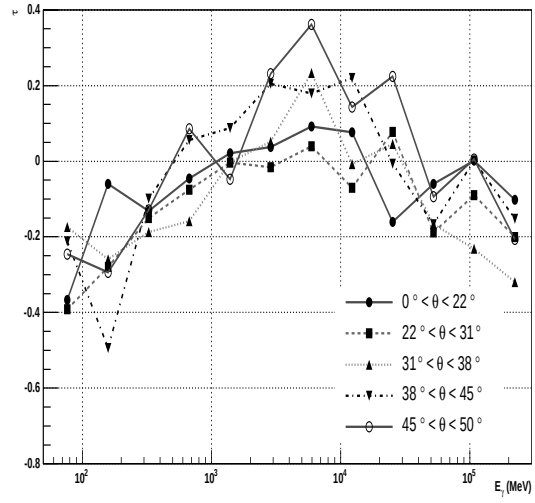

Figure 57: Parametric method's tail for thick strips.

Appendix C: **Estimating the Effective Area**

The method's effective area is calculated as a function of E_γ and θ. The calculations are performed by counting events going through the horizontal plane $z = 0\,\mathrm{mm}$. The plane is divided in $40\,\mathrm{mm}$ square tiles and separate counts $C(x^i, y^i)$ for each one. The counting is performed twice:

1. All events, whether or not they trigger or even convert in the detector. These events counts are named $C(x^i, y^i)$. Their sum is the number of simulated events.
2. Good events, defined as the ones passing all of the following cuts:
   - Onboard filter status is null, i.e. event was not rejected.
   - At least one reconstructed track in the TKR.
   - $Q_\gamma > 10\,\mathrm{MeV}$.
   - $|\frac{\tilde{E}_\gamma - E_\gamma}{E_\gamma}| < \delta$. The latter parameter is defined as $\delta = 0.1$ on Fig. 40, $\delta = 0.5$ on Fig. 41.

   These counts are named $\tilde{C}(x^i, y^i)$.

The ratio of good to all events $\frac{\tilde{C}(x^i,y^i)}{C(x^i,y^i)}$ is an estimation of the detector efficiency for tile (x^i, y^i). This ratio times the tile area is an estimation of the effective area for that tile. The effective area is then:

$$A^{Eff} = \sum_{x^i,y^i} \frac{\tilde{C}(x^i, y^i)}{C(x^i, y^i)} \cdot 40 \cdot 40\,\mathrm{mm}^2 \tag{13}$$

Appendix D: **The Lognormal**

Mathematically, a variable X is lognormally distributed when the variable $\log X$ is normally distributed. In practice, the lognormal is a gaussian with an asymetric tail. The expression used here is somewhat adapted from the mathematical definition:

$$\mathrm{logN}(x) = N \exp\left(-\frac{\bar{x}^2 + \tau^2}{2}\right) \tag{14}$$

using:

$$N = \frac{1}{\sigma\sqrt{2\pi}} \frac{\sinh\left(\tau\sqrt{\log 4}\right)}{\tau\sqrt{\log 4}}$$
$$\bar{x} = \frac{\log\left(1 + \frac{x-\mu}{\sigma}\frac{\sinh\left(\tau\sqrt{\log 4}\right)}{\sqrt{\log 4}}\right)}{\tau}$$

where:

- N is the normalisation term so that $\int \mathrm{logN} = 1$.
- μ is the MPV.
- σ is the width. Conveniently, 2.36σ is the FWHM.
- τ is the tail parameter. For $\tau = 0$ the distribution becomes a gaussian.

The cumultive distribution is:

$$\int_x^{+\infty} \mathrm{logN} dx = N\mathrm{erf}(\left(\frac{\bar{x} - \tau}{\sqrt{2}}\right) \tag{15}$$

using:

$$\mathrm{erf}(x) = \frac{2}{\sqrt{\pi}} \int_x^{+\infty} \exp\left(-t^2\right) dt$$